

# MoS<sub>2</sub> Quantum Dot/Graphene Hybrids for Advanced Interface Engineering of a CH<sub>3</sub>NH<sub>3</sub>PbI<sub>3</sub> Perovskite Solar Cell with an Efficiency of over 20%

Leyla Najafi,<sup>†,‡</sup> Babak Taheri,<sup>‡,§</sup> Beatriz Martín-García,<sup>†</sup> Sebastiano Bellani,<sup>†</sup> Diego Di Girolamo,<sup>‡</sup> Antonio Agresti,<sup>‡</sup> Reinier Oropesa-Nuñez,<sup>†,||</sup> Sara Pescetelli,<sup>‡</sup> Luigi Vesce,<sup>‡</sup> Emanuele Calabrò,<sup>‡</sup> Mirko Prato,<sup>⊥</sup> Antonio E. Del Rio Castillo,<sup>†</sup> Aldo Di Carlo,<sup>\*,‡,§,||</sup> and Francesco Bonaccorso<sup>\*,†,||</sup>

<sup>†</sup>Graphene Labs, Istituto Italiano di Tecnologia, Via Morego 30, 16163 Genova, Italy

<sup>‡</sup>C.H.O.S.E. (Centre for Hybrid and Organic Solar Energy), Department of Electronic Engineering, University of Rome Tor Vergata, Via del Politecnico 1, 00133 Rome, Italy

<sup>||</sup>BeDimensional Srl., Via Albisola 121, 16163 Genova, Italy

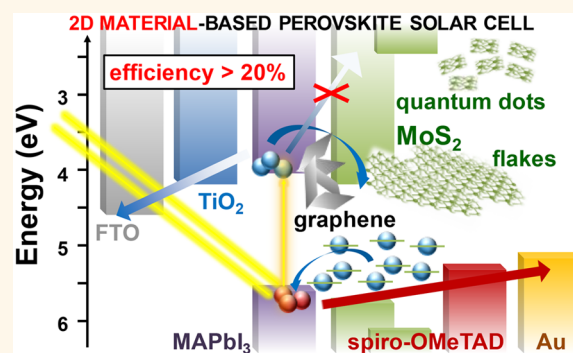
<sup>⊥</sup>Materials Characterization Facility, Istituto Italiano di Tecnologia, Via Morego 30, 16163 Genova, Italy

<sup>§</sup>L.A.S.E.—Laboratory for Advanced Solar Energy, National University of Science and Technology “MISiS”, Leninskiy Prosect 6, 119049 Moscow, Russia

## Supporting Information

**ABSTRACT:** Interface engineering of organic–inorganic halide perovskite solar cells (PSCs) plays a pivotal role in achieving high power conversion efficiency (PCE). In fact, the perovskite photoactive layer needs to work synergistically with the other functional components of the cell, such as charge transporting/active buffer layers and electrodes. In this context, graphene and related two-dimensional materials (GRMs) are promising candidates to tune “on demand” the interface properties of PSCs. In this work, we fully exploit the potential of GRMs by controlling the optoelectronic properties of molybdenum disulfide (MoS<sub>2</sub>) and reduced graphene oxide (RGO) hybrids both as hole transport layer (HTL) and active buffer layer (ABL) in mesoscopic methylammonium lead iodide (CH<sub>3</sub>NH<sub>3</sub>PbI<sub>3</sub>) perovskite (MAPbI<sub>3</sub>)-based PSCs. We show that zero-dimensional MoS<sub>2</sub> quantum dots (MoS<sub>2</sub> QDs), derived by liquid phase exfoliated MoS<sub>2</sub> flakes, provide both hole-extraction and electron-blocking properties. In fact, on one hand, intrinsic n-type doping-induced intraband gap states effectively extract the holes through an electron injection mechanism. On the other hand, quantum confinement effects increase the optical band gap of MoS<sub>2</sub> (from 1.4 eV for the flakes to >3.2 eV for QDs), raising the minimum energy of its conduction band (from −4.3 eV for the flakes to −2.2 eV for QDs) above the one of the conduction band of MAPbI<sub>3</sub> (between −3.7 and −4 eV) and hindering electron collection. The van der Waals hybridization of MoS<sub>2</sub> QDs with functionalized reduced graphene oxide (f-RGO), obtained by chemical silanization-induced linkage between RGO and (3-mercaptopropyl)trimethoxysilane, is effective to homogenize the deposition of HTLs or ABLs onto the perovskite film, since the two-dimensional nature of RGO effectively plugs the pinholes of the MoS<sub>2</sub> QD films. Our “graphene interface engineering” (GIE) strategy based on van der Waals MoS<sub>2</sub> QD/graphene hybrids enables MAPbI<sub>3</sub>-based PSCs to achieve a PCE up to 20.12% (average PCE of 18.8%). The possibility to combine quantum and chemical effects into GIE, coupled with the recent success of graphene and GRMs as interfacial layer, represents a promising approach for the development of next-generation PSCs.

**KEYWORDS:** perovskite solar cells, 2D materials, graphene, molybdenum disulfide (MoS<sub>2</sub>), quantum dots, interface engineering



Organic–inorganic halide perovskite solar cells (PSCs) are in the spotlight of photovoltaic (PV) research to rival the leading technologies<sup>1–4</sup> (i.e., crystalline

Received: July 22, 2018

Accepted: September 13, 2018

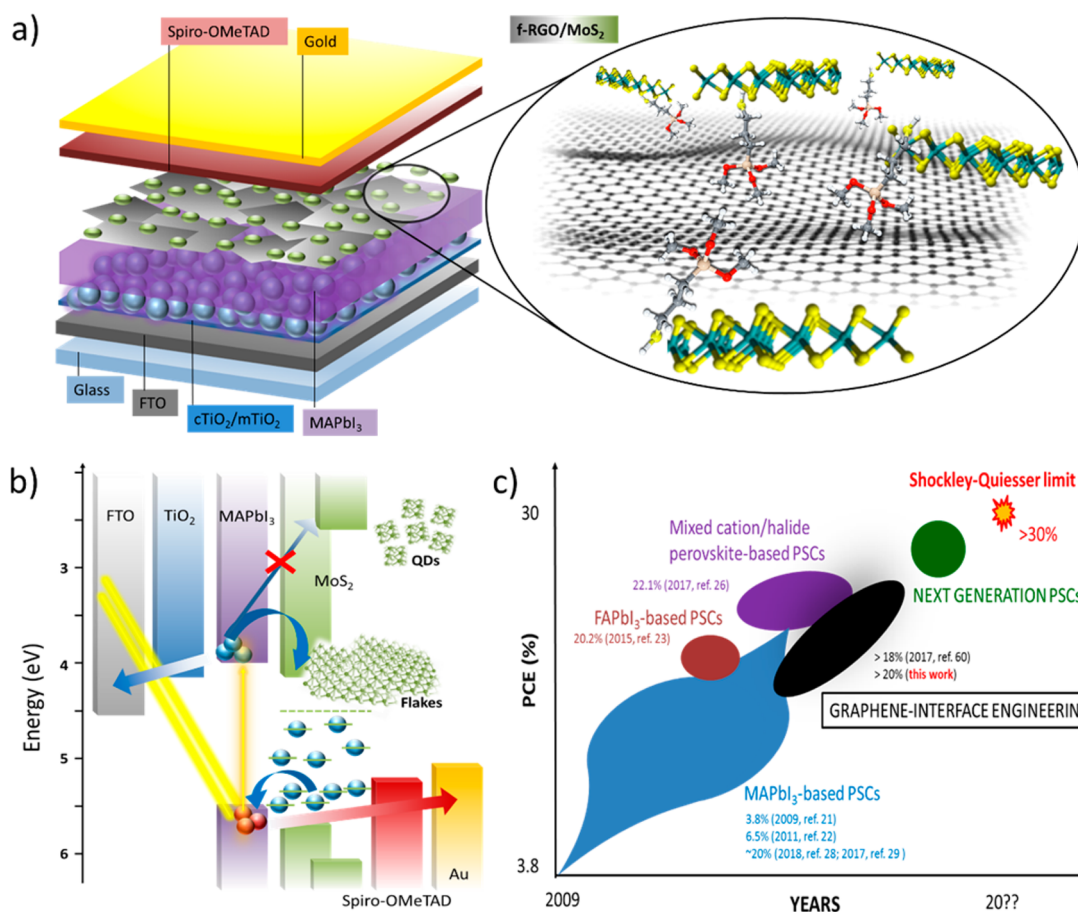


**Figure 1.** (a) Sketch of mesoscopic MAPbI<sub>3</sub>-based PSC exploiting MoS<sub>2</sub> QDs:f-RGO hybrids as both HTL and ABL. (b) Scheme of the energy band edge positions of the materials used in the different components of the assembled mesoscopic MAPbI<sub>3</sub>-based PSC. The energy band edge positions of MoS<sub>2</sub> flakes and MoS<sub>2</sub> QDs were determined from OAS and UPS measurements detailed in the text, while those of the other materials were taken from the literature: FTO,<sup>52</sup> TiO<sub>2</sub>,<sup>52</sup> MAPbI<sub>3</sub>,<sup>134–139</sup> Spiro-OMeTAD,<sup>52</sup> and Au.<sup>52</sup> (c) State-of-the-art and predicted PCE evolution for PSCs, highlighting the synergistic potential of GIE and the formulation of advanced perovskite chemistries.

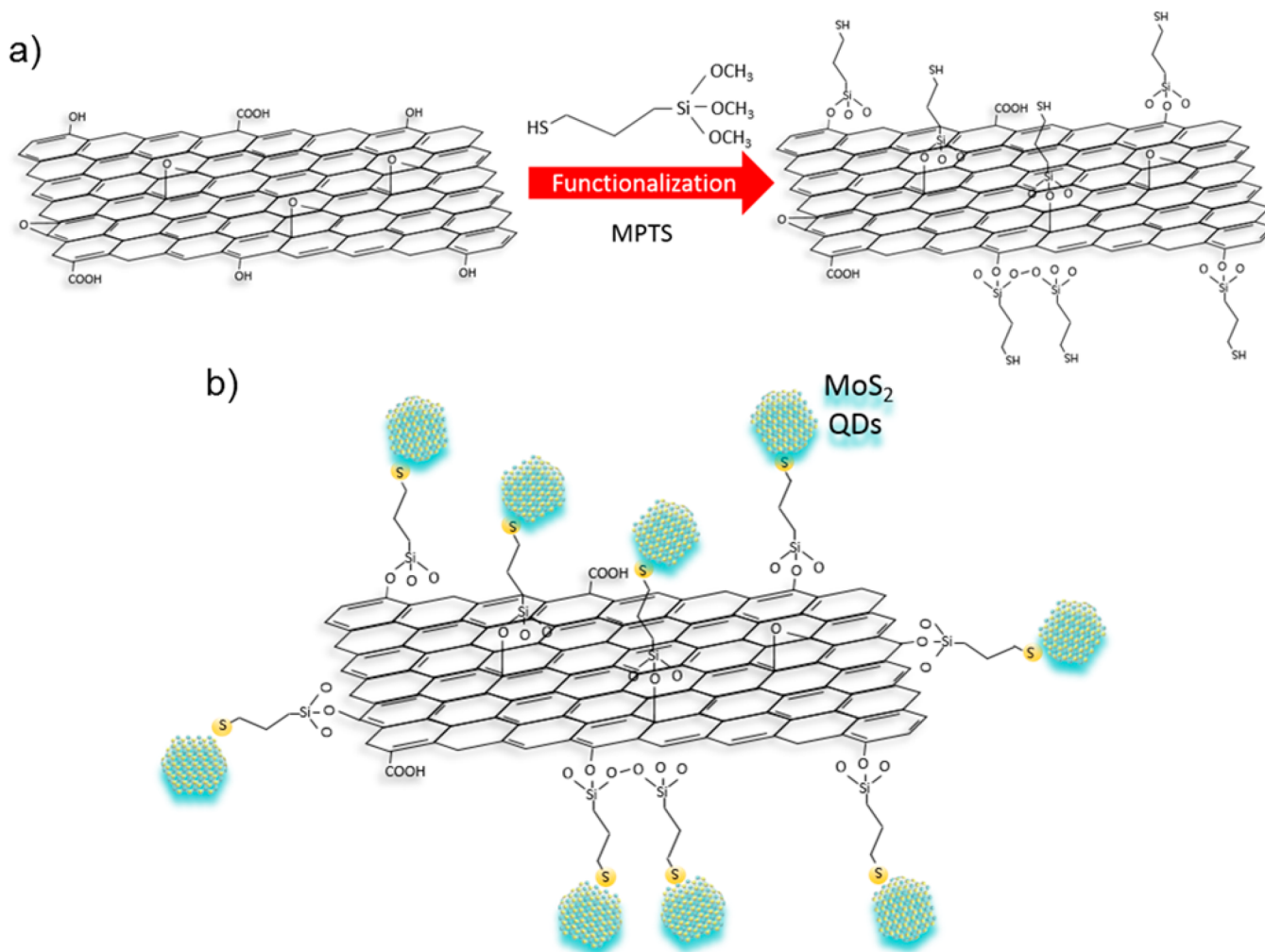
silicon solar cells<sup>5–7</sup> and inorganic thin-film solar cells<sup>8,9</sup> since power conversion efficiency (PCE) exceeding 20%<sup>10–12</sup> can be obtained by affordable (low-cost and low-temperature) solution processing<sup>13–15</sup> with a scaling-up prospective.<sup>16–19</sup>

Methylammonium lead iodide (CH<sub>3</sub>NH<sub>3</sub>PbI<sub>3</sub>) perovskite (MAPbI<sub>3</sub>) has been intensively studied as light-harvesting material from the beginning of PSC development,<sup>1,2,20–22</sup> and the elemental composition engineering of its chemistry<sup>23,24</sup> led to mixed cation and halide PSCs,<sup>25</sup> which boosted the certified PCE above 22% (*i.e.*, 22.1%<sup>26</sup> and 22.7%<sup>10</sup>). Although the archetypal MAPbI<sub>3</sub> reached a certified maximum efficiency of 19.3%<sup>27</sup> (uncertified efficiency exceeding 20%<sup>28–31</sup>), it still has a benchmarking role for the optimization and/or validation of PSC architectures<sup>31–34</sup> due to its historical breakthrough in PV technology over the last years (starting from 2009, with a PCE of 3.8%<sup>21</sup>).<sup>10</sup> In particular, MAPbI<sub>3</sub>-based PSCs provide a platform to study and design the interfaces between each functional layer of the PSCs,<sup>16,35–41</sup> whose carrier transport barriers determine undesirable hysteresis and instability effects in PSCs,<sup>33,42–44</sup> both in mesoscopic<sup>31,45</sup> and planar structures.<sup>45</sup> In fact, the photogenerated carriers have to be transported across the interfaces in the PSC structure,<sup>38,46–48</sup> and charge loss can occur due to energy barriers and/or interfacial defects.<sup>38,46–48</sup> Therefore, appropriate energy level tailoring at the interfaces is pivotal in (1) increasing open circuit voltage ( $V_{oc}$ ); (2) facilitating charge transfer and

extraction,<sup>49,50</sup> which contribute to increase the short circuit current ( $J_{sc}$ ) and fill factor (FF);<sup>49,50</sup> (3) eliminating hysteresis phenomena;<sup>51–53</sup> and (4) extending the lifetime.<sup>54,55</sup> In the run-up to reach the theoretical PCE limit ( $\sim 31\%$ )<sup>56</sup> of PSCs (practical limits of 29.5%<sup>57</sup> with value of 30.5%,<sup>58</sup> which have also been reported by considering intrinsic nonradiative recombination processes), graphene and related two-dimensional (2D) materials (GRMs) are emerging as a paradigm shift of interface engineering to boost the PV performance.<sup>56,59–73</sup> Actually, the large variety of GRMs offers peculiar (opto)electronic properties<sup>74,75</sup> that can be tuned on-demand by means of morphological modification<sup>76,77</sup> and chemical functionalization.<sup>78–80</sup> Moreover, GRMs can be produced from the exfoliation of their bulk counterpart in suitable solvents<sup>81–85</sup> as functional inks.<sup>86</sup> The latter can be deposited on different substrates by established large-scale, cost-effective printing/coating techniques,<sup>87–90</sup> compatible with solution-based manufacturing of PSCs.<sup>15,91–93</sup>

With the aim to deeply exploit the use of 2D materials for engineering the interface of PSCs, herein we report a synergistic quantum-chemical approach for controlling the energy band levels and the thin-film morphology of low-dimensional, van der Waals hybrids between molybdenum disulfide quantum dots (MoS<sub>2</sub> QDs) and reduced graphene oxide (RGO) as hole transport layer (HTL) or active buffer layer (ABL) (between the HTL and Au electrode) in

Scheme 1. Representative sketches of (a) the functionalization of RGO (structure based on the Lerf–Klinowski model)<sup>186</sup> with MPTS; (b) the hybridization of MoS<sub>2</sub> QDs and f-RGO.



mesoscopic MAPbI<sub>3</sub>-based PSCs (Figure 1a). Notably, both 2D MoS<sub>2</sub> and RGO have been previously reported as possible HTLs<sup>64,72,94–103</sup> or ABLs.<sup>64,104,105</sup> However, their intrinsic work function (WF) (typically <4.8 eV for both pristine MoS<sub>2</sub><sup>106–109</sup> and RGO<sup>110–113</sup>) is inferior to that of conventional HTL materials, including 2,2',7,7'-tetrakis(*N,N*-di-4-methoxyphenylamino)-9,9'-spirofluorene (spiro-OMeTAD) (WF > 4.9,<sup>114,115</sup> especially for the doped forms mostly exploited as HTLs<sup>114–117</sup>) and poly(3,4-ethylenedioxythiophene):poly(styrenesulfonate) (PEDOT:PSS) (WF ranging between 5.0 and 5.2 eV<sup>118–121</sup>). This can limit the hole extraction process.<sup>95,122,123</sup> Moreover, the optical band gap ( $E_g$ ) of both RGO (<2 eV,<sup>124,125</sup> depending on its oxidation level<sup>124,125</sup>) and MoS<sub>2</sub> (~1.2 eV for bulk<sup>126,127</sup> and ~1.8 eV for single-layer<sup>128–130</sup>) results in a minimum energy of the conduction band (CB) (~4.3 eV<sup>131–133</sup>) lower than that of the lowest unoccupied molecular orbital (LUMO) (reported between -4.0<sup>134–137</sup> and -3.7 eV<sup>114,138,139</sup>), not providing electron-blocking properties.<sup>140,141</sup> Therefore, physical/chemical modification of 2D MoS<sub>2</sub> and RGO are needed to tune the optoelectronic properties for their efficient implementation as HTLs.<sup>95,99,110,122,123,142,143</sup> As shown in Figure 1b, a zero-dimensional (0D) anodic interlayer of MoS<sub>2</sub> QDs, derived by liquid phase exfoliation (LPE) of

MoS<sub>2</sub> flakes,<sup>144</sup> hold optimal electronic structure to effectively extract the photogenerated holes through an electron injection mechanism<sup>145–147</sup> from their intrinsic n-type doping<sup>148–151</sup>-induced intraband gap states.<sup>152,153</sup> The latter have been reported to be a consequence of the natural presence in MoS<sub>2</sub> of sulfur vacancies,<sup>153–158</sup> impurities,<sup>159,160</sup> and defects.<sup>161–164</sup> Quantum confinement effects open the MoS<sub>2</sub> optical band gap (from 1.4 eV for the flakes to >3.2 eV for the QDs), raising the minimum energy of the CB of MoS<sub>2</sub> (from -4.3 eV for the flakes to -2.2 eV for the QDs) above the energy of the LUMO of MAPbI<sub>3</sub> (between -4.0<sup>134–137</sup> and -3.7 eV<sup>114,138,139</sup>), thus blocking electron injection in HTL. Hole-extraction and electron-blocking properties of MoS<sub>2</sub> QDs synergistically suppress the interfacial charge recombination losses observed in benchmark devices (fluorine-doped tin oxide (FTO)/compact TiO<sub>2</sub> (cTiO<sub>2</sub>)/mesoporous TiO<sub>2</sub> (mTiO<sub>2</sub>)/MAPbI<sub>3</sub>/2,2',7,7'-tetrakis(*N,N*-di-4-methoxyphenylamino)-9,9'-spirobi-fluorene (spiro-OMeTAD)/Au),<sup>34,165</sup> and in previous cell architectures exploiting native MoS<sub>2</sub> flakes as ABLs.<sup>64,165</sup> With the aim to form homogeneous (*i.e.*, pinhole-free) nanometer-thick HTLs, MoS<sub>2</sub> QDs, which do not cover totally the MAPbI<sub>3</sub> film after their deposition, are hybridized with chemically (3-mercaptopropyl)trimethoxysilane (MPTS)-functionalized RGO (f-RGO) flakes<sup>166</sup> (named MoS<sub>2</sub> QDs:f-

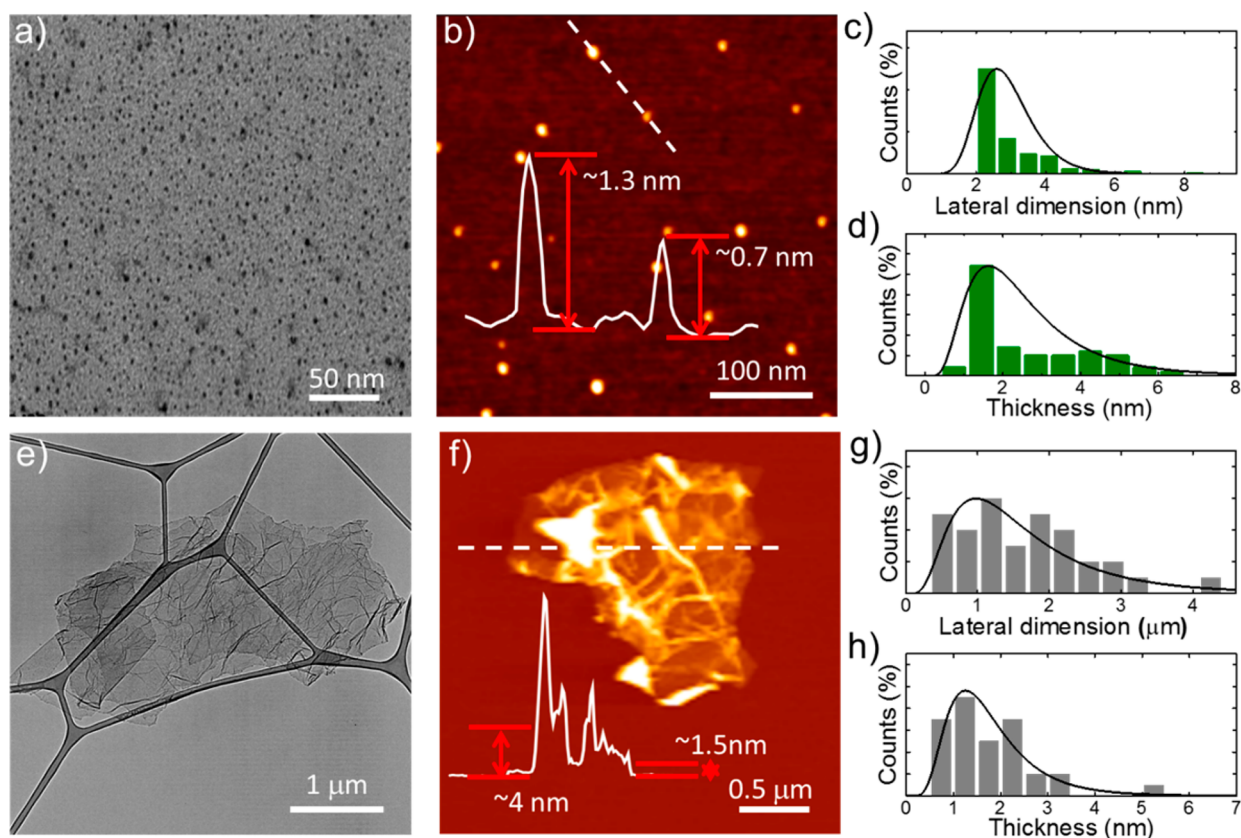


**Figure 2.** Morphological characterization of (a–d) the as-produced MoS<sub>2</sub> QDs and (e–h) f-RGO flakes. TEM and AFM images of (a, b) MoS<sub>2</sub> QDs and (e, f) f-RGO and the corresponding statistical analysis of (c, g) the lateral dimension and (d, h) the thickness, respectively. The statistical analyses were performed on 50 flakes from the different images collected. Representative height profiles (solid white lines) of the indicated sections (white dashed lines) are also shown in panels (b) and (f).

RGO). The RGO flakes are effective to plug the pinholes in MoS<sub>2</sub> QDs films, thus to homogenize the HTL. The choice of the functionalization for RGO relies on the bifunctional role of MPTS molecules, which effectively anchor onto the RGO flakes (*via* silanization-mediated bonding),<sup>167,168</sup> while exposed thiol (SH) moieties enable f-RGO to interact with MoS<sub>2</sub> QDs (*via* S–S van der Waals physisorption<sup>169</sup> and/or S-vacancies passivation/filling<sup>170,171</sup>). Our results show the potential of quantum and chemical effects in “graphene interface engineering” (GIE) to produce highly performant MAPbI<sub>3</sub>-based PSCs with a PCE up to 20.12% (average PCE of 18.8%). The remarkable advances achieved also in the exploitation of graphene flake- and graphene QD-doped ETLs, including both mesoscopic TiO<sub>2</sub><sup>45</sup> and solution-processed SnO<sub>2</sub>,<sup>28</sup> make GIE a versatile tool for the design of record-high efficiency (solution-processed) next-generation PSCs (Figure 1c).

## RESULTS AND DISCUSSION

**Production and Characterization of MoS<sub>2</sub> QDs, f-RGO, and MoS<sub>2</sub> QDs:f-RGO.** The MoS<sub>2</sub> QDs were produced through a facile and scalable one-step solvothermal approach starting from MoS<sub>2</sub> flakes previously obtained by LPE of bulk MoS<sub>2</sub> in 2-propanol (IPA),<sup>144</sup> followed by a sedimentation-based separation (SBS) process.<sup>172,173</sup> The LPE process exploits hydrodynamic shear-force-controlled ultrasonication to overcome the van der Waals forces (15–20 meV Å<sup>-2</sup>,<sup>174</sup> or ~5 meV/atom,<sup>175,176</sup>) that bind MoS<sub>2</sub> layers.<sup>81,84,177,178</sup> The SBS process separates various particles on the basis of their sedimentation rate in response to a centrifugal force acting on

them.<sup>84,179</sup> Subsequently, the so-produced MoS<sub>2</sub> flakes were first produced by LPE and then solvothermally treated for the production of MoS<sub>2</sub> QDs.<sup>144</sup> Then, by exploiting SBS we selected MoS<sub>2</sub> QDs, while residual MoS<sub>2</sub> flakes were discarded as sediment.<sup>144</sup> Reduced graphene oxide was produced by thermal annealing (1000 °C under a 100 sccm flow of Ar (90%):H<sub>2</sub> (10%)) of graphene oxide (GO)<sup>180,181</sup> synthesized from graphite flakes using a modified Hummer’s method.<sup>182</sup> Subsequently, RGO was functionalized by MPTS *via* silanization-mediated chemical bonding.<sup>166,183</sup> The silanization process was triggered by the hydrolyzation and condensation of the methoxy groups (–OCH<sub>3</sub>) of MPTS, which react with the O moieties of RGO (Scheme 1a).<sup>166,167</sup> A solvent-exchange process<sup>95,184,185</sup> was carried out to redisperse MoS<sub>2</sub> QDs and f-RGO dispersions in IPA. The hybrid MoS<sub>2</sub> QDs:f-RGO dispersion was obtained by mixing f-RGO and MoS<sub>2</sub> QD dispersions with a material weight ratio of 1:2. The hybridization of the materials is completed by the exposed SH moieties of f-RGO, which interact with MoS<sub>2</sub> QDs *via* S–S van der Waals physisorption<sup>169</sup> and/or passivation/filling of the S-vacancies of MoS<sub>2</sub> QDs<sup>170,171</sup> (Scheme 1b).

The details of material production and dispersion formulation are reported in the [Experimental Methods](#) section. It is worth noting that the final material dispersions were obtained in low boiling-point alcohol-based solvents, which are compatible with environmentally friendly, low-temperature, and solution-processed material deposition methods. By taking advantage of this approach, we exploited spray-coating deposition, since it can be applied on irregular surfaces with

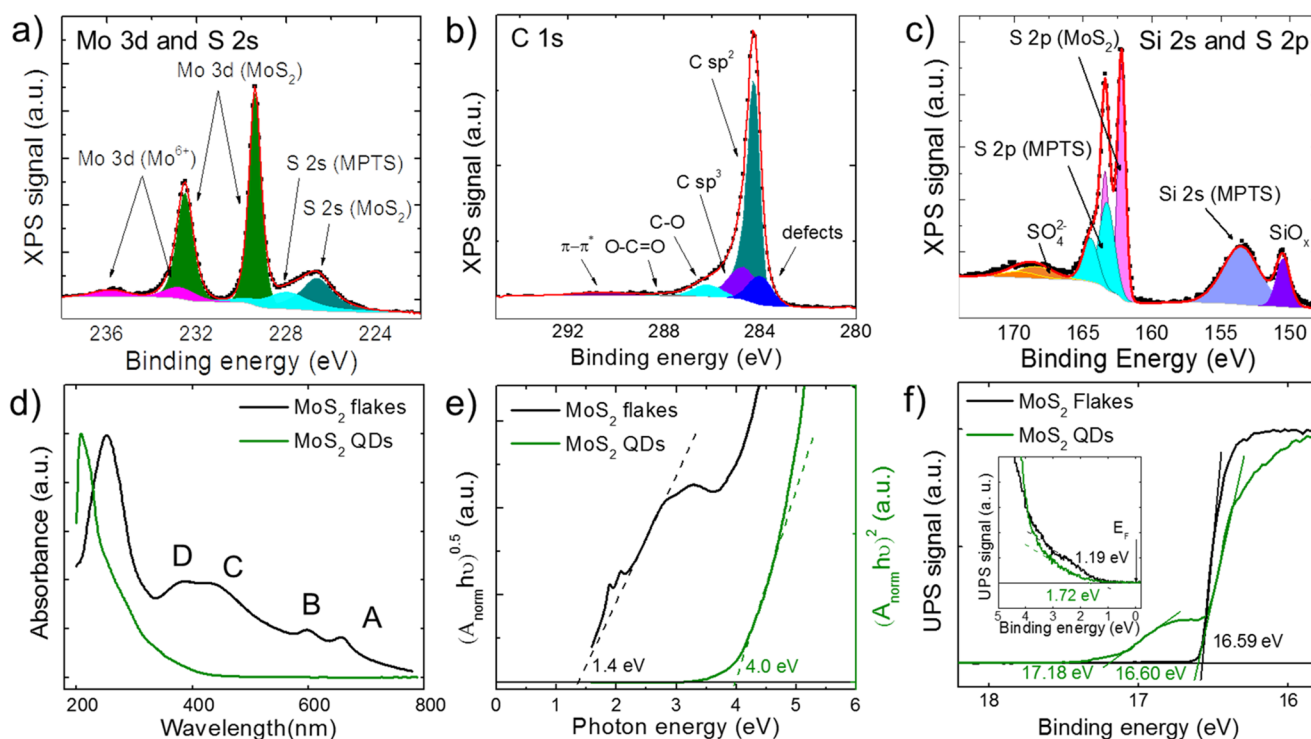


**Figure 3.** (a) Mo 3d and S 2s, (b) C 1s and (c) Si 2s and S 2p XPS spectra for MoS<sub>2</sub> QDs:f-RGO. The deconvolution of the corresponding XPS spectra is also shown. (d) Absorption spectra of MoS<sub>2</sub> flakes and QDs. (e) Tauc plots of MoS<sub>2</sub> flakes and QDs. (f) Secondary electron threshold region of He-I UPS spectra of MoS<sub>2</sub> flakes and QDs, which were used for estimating the WF values. The inset shows VB region of He-I UPS spectra of MoS<sub>2</sub> flakes and QDs used for estimating  $E_F$  values. The shoulder observed in MoS<sub>2</sub> QDs UPS spectrum can be attributed to the presence of defective species (edge/S-vacancies) in a polydispersed sample.

higher reproducibility than that obtained with other deposition methods (e.g., spin/blade coating and screen printing).<sup>187</sup> Moreover, with a broader context vision, spray coating is a promising technique to speed up the production of perovskite module fabrication<sup>188,189</sup> in view of their market entry.<sup>190,191</sup>

The lateral size and thickness of the as-produced MoS<sub>2</sub> QDs and f-RGO samples were evaluated by means of transmission electron microscopy (TEM) and atomic force microscopy (AFM), respectively. Figure 2a,b show representative TEM and AFM images of MoS<sub>2</sub> QDs. Microscopy statistical analyses of lateral dimension (Figure 2c) and thickness (Figure 2d) show log-normal distributions peaking at  $\sim 2.6$  and  $\sim 1.6$  nm, respectively, which means that both one- and few-layer QDs were effectively produced (the monolayer thickness is between 0.7 and 0.8 nm<sup>128,192</sup>). Notably, the thickness distribution of MoS<sub>2</sub> QDs is similar to that measured for the native MoS<sub>2</sub> flakes (average thickness of  $\sim 2.7$  nm), whose morphological characterization is reported in the Supporting Information (SI) (Figure S1). Figure 2e,f report TEM and AFM images of f-RGO flakes, exhibiting an irregular shape and rippled paper-like morphology. Microscopy statistical analyses of lateral dimension (Figure 2g) and thickness (Figure 2h) display a log-normal distributions peaked at  $\sim 980$  and  $\sim 1.3$  nm, respectively. These values are comparable with those obtained for native RGO (average lateral dimension and thickness of 1.7  $\mu\text{m}$  and 1.8 nm, respectively)<sup>183</sup> (see Figure S2). Since the thickness of single-layer pristine graphene is  $\sim 0.34$  nm,<sup>193,194</sup> these data indicated that our methodology produced few-layer f-RGO flakes. The structural properties of the materials were investigated by Raman spectroscopy (see SI for additional Raman spectroscopy analysis details, Figure S3), confirming their exfoliated crystal structure.

X-ray photoelectron spectroscopy (XPS) measurements were carried out to determine the elemental composition, chemical phase, and interaction of the as-produced MoS<sub>2</sub> QDs:f-RGO samples. Figure 3a shows the S 2s and Mo 3d XPS spectra of MoS<sub>2</sub> QDs:f-RGO, together with their deconvolution. The peaks at the lowest binding energy ( $\sim 226$  eV) and the peak at  $\sim 229$  eV are assigned to S 2s<sup>144,195,196</sup> and Mo 3d<sub>5/2</sub>, respectively, of the semiconducting 2H (trigonal prismatic) phase of MoS<sub>2</sub>.<sup>144,195,196</sup> The peak centered at  $\sim 232.5$  eV can be fitted with two components.<sup>64,144</sup> The first component ( $\sim 232$  eV) is assigned to Mo 3d<sub>3/2</sub> of the 2H-MoS<sub>2</sub>. Instead, the second one ( $\sim 233$  eV), as well as the low-intensity peak centered at  $\sim 236$  eV, is associated with oxidized phases of Mo,<sup>177,197</sup> which can be produced during the LPE of bulk MoS<sub>2</sub>.<sup>144,177</sup> However, the percentage content (%c) of oxidized Mo (<3%) indicates that only a small fraction of the material is oxidized. Noteworthy, the initial LPE step in IPA can overcome the drawbacks of the LPE of transition metal dichalcogenides<sup>144,198</sup> (including MoS<sub>2</sub><sup>144</sup>) in conventional high boiling-point solvents, such as *N*-methyl-2-pyrrolidone (NMP)<sup>64,177,178,199</sup> and *N,N*-dimethylformamide (DMF),<sup>64,177,178</sup> where high percentage contents of oxidized species (between 40% and 60%, depending on the process parameter) are typically produced.<sup>64,177</sup> Moreover, the functionalization process did not cause any additional oxidation of MoS<sub>2</sub> QDs, since the %c of oxidized Mo in the hybrids (<3%) is also comparable to that of both MoS<sub>2</sub> flakes (<7%)<sup>144</sup> and MoS<sub>2</sub> QDs ( $\sim 5\%$ ).<sup>144</sup> The component at  $\sim 228$  eV appearing in the S 2s XPS spectrum is ascribed to the presence of S moieties of f-RGO and proves the interaction of the MPTS functionalization with MoS<sub>2</sub> QDs via S–S van der Waals physisorption<sup>169</sup> and/or passivation/

filling of the S-vacancies of MoS<sub>2</sub> QDs,<sup>170,171</sup> as proposed in Scheme 1b. The ratio between % of Mo 3d and S 2s ascribed to MoS<sub>2</sub> QDs is <0.5, while for the MoS<sub>2</sub> QDs the same ratio was >0.5.<sup>144</sup> This suggests that the functionalization process could restore the S-vacancies of the native MoS<sub>2</sub>, in agreement with the hybridization mechanism reported in Scheme 1b.

Figure 3b shows the C 1s spectrum of MoS<sub>2</sub> QDs:f-RGO, which is deconvoluted in six components, indicating the C sp<sup>2</sup> and sp<sup>3</sup> network and oxygen functionalities of the f-RGO.<sup>200</sup> The C sp<sup>2</sup> component, centered at 284.5 eV, dominates the spectrum (%c ≈ 57%), indicating that the delocalized  $\pi$ -conjugated structure was almost fully restored after the thermal reduction of the native GO (%c of C sp<sup>2</sup> ≈ 48.5%).<sup>183,201,202</sup> The component peaking at ~286.2 eV is assigned to C–O bonds (%c = 7.7%). A residue of C sp<sup>3</sup> is still present (peak centered at 284.7 eV, %c ≈ 20.3%) as well as carboxylate carbon O–C=O bonds (peak centered at 287.7 eV, %c ≈ 1%). The component observed at ~290.7 eV is attributed to  $\pi$ – $\pi^*$  satellite structure (extended delocalized electrons),<sup>203,204</sup> a characteristic of aromatic C structure. The component peaking at 284.0 eV is also significantly present (%c ~ 14%). This band can arise as a consequence of C lattice vacancies/distortions introduced mainly during the GO reduction process<sup>183</sup> and/or the hybridization of f-RGO with MoS<sub>2</sub> QDs. Regarding the MPTS functionalization of the RGO, Figure 3c shows the Si 2s and S 2p XPS spectra, together with their deconvolution. The appearance of the silane and S-doublet components peaking at ~153.5 and ~163.3 eV, respectively,<sup>166,205</sup> are fingerprints of the MPTS. The components peaking at ~168.4 and ~169.7 eV are attributed to a S 2p doublet of SO<sub>4</sub><sup>2-</sup>.<sup>166,206</sup> These oxidized species are due to both MPTS interacting with O moieties on RGO flakes<sup>167,207</sup> and MPTS oxidized during the functionalization process. The %c of the oxidized groups is ~5% of the total S content. The ratio between the S content related to the MPTS and the C sp<sup>2</sup> of f-RGO is 3% and estimates the percentage extent of the functionalization of RGO with MPTS.<sup>183</sup> The interaction between the MPTS and the RGO flakes was confirmed by complementary Fourier-transform infrared (FTIR) measurements. After RGO functionalization, in the f-RGO FTIR spectrum (see SI, Figure S4), the Si–O–Si stretching band appears at 1078 cm<sup>-1</sup>, shifted and broadened compared to pure MPTS (1089 cm<sup>-1</sup>), indicating the coupling between the alkoxy silane groups and the oxygen groups of RGO, as proposed in Scheme 1. Even more, the Si–O–Si band is still present in MoS<sub>2</sub> QDs:f-RGO, keeping the same position. This indicated that no modification occurred in the silane–RGO interaction path, leaving only the SH groups as a linker option for the MoS<sub>2</sub> QDs (see the SI for further discussion). The effectiveness of the MPTS functionalization was also macroscopically observed by noting the improved dispersibility of f-RGO in ethanol compared to that of RGO (Figure S5). In fact, MPTS are polar molecules able to decrease the surface energy of native RGO in alcohol-based solvents (~46.1 mN m<sup>-1</sup> in ethanol),<sup>208,209</sup> enhancing dispersion stability and hindering formation of aggregates during film deposition.<sup>183</sup> In addition, XPS analysis also evidences that in the same energy range, the S 2p doublet due to MoS<sub>2</sub> QDs is also present at 162.2 eV.

Optical absorption spectroscopy (OAS) and ultraviolet photoelectron spectroscopy (UPS) measurements were carried out in order to assess the charge-extraction/blocking capability of MoS<sub>2</sub> QDs. Native MoS<sub>2</sub> flakes were also measured for

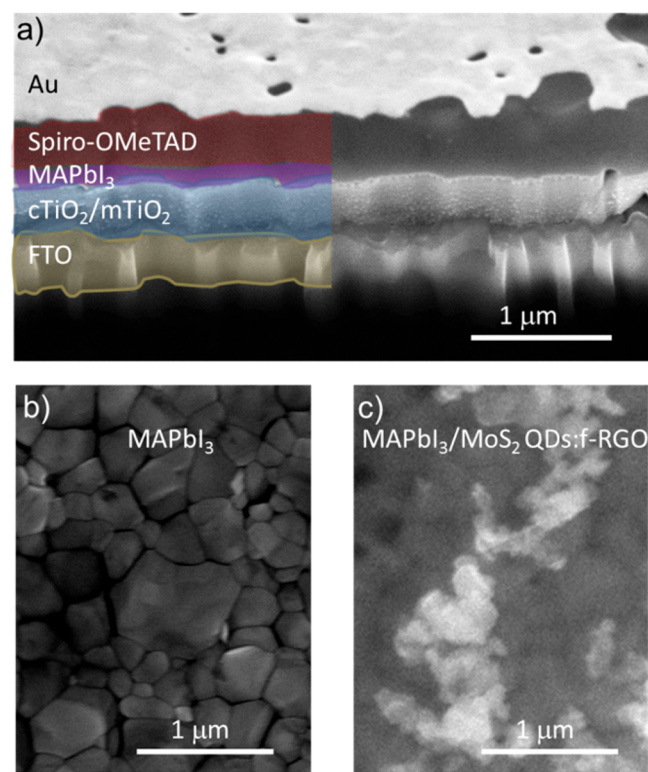
comparison, since they have been previously reported as effective ABLs between MAPbI<sub>3</sub> and spiro-OMeTAD in mesoscopic PSCs.<sup>64</sup> The UV–vis absorption spectrum of MoS<sub>2</sub> flakes (Figure 3d) shows peaks at ~670 and ~620 nm, which arise from the excitonic transitions, (known as A and B, respectively) the split valence bands and the minima of the conduction band at the K-point of the Brillouin zone of layered MoS<sub>2</sub>.<sup>210,211</sup> More in detail, the spin–orbit interaction and interlayer coupling are responsible for the valence band (VB) splitting. The energy difference between the A and B transitions is ~180 meV, which agrees with the values predicted by density functional theory (DFT) calculations (146 and 174 meV for monolayer and bilayer, respectively).<sup>212</sup> The broad absorption band centered at ~400 nm arises from the C and D interband transitions between the density of state peaks in the valence and conduction bands.<sup>213,214</sup> Differently, MoS<sub>2</sub> QDs do not show the absorption peaks of MoS<sub>2</sub> flakes, and their absorption edge shifts toward lower wavelength compared to the latter. This is a consequence of quantum 0D confinement,<sup>215,216</sup> which affects the optical properties of nanostructures when their size is comparable to or smaller than the excitonic Bohr radius (~23 nm for MoS<sub>2</sub>).<sup>217</sup> Quantum confinement, as well as edge effects, endow excitation-dependent photoluminescence (PL) properties in MoS<sub>2</sub> QDs (Figure S6).<sup>144,215,218,219</sup> In fact, the PL emission peak of MoS<sub>2</sub> QDs is red-shifted with increasing excitation wavelength.<sup>144</sup> In order to further confirm the effect of quantum confinement on the optical properties of MoS<sub>2</sub>, the  $E_g$  was evaluated by the  $(ah\nu)^n$  vs  $h\nu$  (Tauc plot) analysis (Figure 3e) using the Tauc relation  $Ah\nu = Y(h\nu - E_g)^n$ , where  $A$  is the absorbance,  $h$  is Planck's constant,  $\nu$  is the photon's frequency, and  $Y$  is a proportionality constant.<sup>220</sup> The value of the exponent denotes the nature of the electronic transition, discriminating between direct-allowed transition ( $n = 2$ ) and indirect-allowed transition ( $n = 0.5$ ).<sup>221</sup> Bulk MoS<sub>2</sub> is an indirect band gap semiconductor with  $E_g = 1.29$  eV.<sup>222</sup> With decreasing thickness, theoretical<sup>223,224</sup> and experimental<sup>128</sup> studies revealed a progressive confinement-induced shift in the indirect band gap from the bulk value of 1.29 eV up to 1.90 eV, while the direct band gap increases by only 0.1 eV.<sup>128</sup> As a consequence of these different scaling properties, MoS<sub>2</sub> undergoes a crossover from an indirect band gap semiconductor to a direct band gap material in the monolayer limit.<sup>128,223,224</sup> The indirect-to-direct band gap transition has a strong impact on the PL emission, which shows a dramatic enhancement (by more than a factor of 1000) compared to that of the bulk counterpart.<sup>225</sup> In the case of our MoS<sub>2</sub> flakes, PL was not detected, in agreement with a dominant few-layer nature evidenced by the AFM statistical analysis of the thickness (Figure 2h). Consequently, in Tauc analysis  $n$  was set equal to 0.5 (indirect-allowed transition). Differently, MoS<sub>2</sub> QDs, although showing similar thickness of the MoS<sub>2</sub> flakes (see Figure 2d,h), display remarkably PL, since additional quantum effects arising from 0D confinement activate direct band gap behavior,<sup>215–217</sup> as proved by PL emission (Figure S6). Then, in Tauc analysis  $n$  was set equal to 2 (direct-allowed transition). It is worth noting that  $n$  undergoes a size (*i.e.*, thickness and lateral dimension)-dependent transition from 2 in direct band gap bulk semiconductors to 1 in a direct band gap nanocrystal.<sup>226</sup> Consequently, the calculated  $E_g$  value of MoS<sub>2</sub> QDs has to be considered qualitatively. Taking into account these considerations, the estimated  $E_g$  increases from ~1.4 eV for MoS<sub>2</sub> flakes to ~4.0 eV (~3.2 eV assuming  $n = 1$ ,

Figure S7) for MoS<sub>2</sub> QDs, in agreement with previous studies.<sup>227</sup>

Ultraviolet photoelectron spectroscopy measurements allowed the Fermi level energy ( $E_F$ ), *i.e.*, the WF, and VB to be determined. Figure 3f shows that secondary electron cutoff (threshold) energies of the He I (21.22 eV) UPS spectra are the same for MoS<sub>2</sub> flakes and QDs ( $\sim 16.8$  eV), corresponding to a WF of  $\sim 4.6$  eV. The inset in Figure 3f shows the UPS spectra region near the  $E_F$ , which allows the maximum energy of the VB to be estimated at  $\sim -5.7$  eV for MoS<sub>2</sub> flakes and  $\sim -6.2$  eV for MoS<sub>2</sub> QDs. Taking into account the  $E_g$  values estimated by Tauc analysis, the minimum energy of the CB is estimated at  $\sim -4.3$  for MoS<sub>2</sub> flakes and  $\sim -2.2$  eV for MoS<sub>2</sub> QDs. The results indicate that, differently from MoS<sub>2</sub> flakes, MoS<sub>2</sub> QDs have a minimum energy of the CB that is lower than that of the LUMO of MAPbI<sub>3</sub> (between  $-4.0$ <sup>134–137</sup> and  $-3.7$  eV<sup>114,138,139</sup>). Consequently, MoS<sub>2</sub> QDs effectively act as electron-blocking material into the PSC structures (see Figure 1b). Furthermore, the UPS data revealed that both MoS<sub>2</sub> flakes and QDs cannot collect holes from their VB, since the corresponding energy levels ( $\sim -5.7$  eV for MoS<sub>2</sub> flakes and  $\sim -6.2$  eV for MoS<sub>2</sub> QDs) are inferior to that of MAPbI<sub>3</sub> ( $\sim -5.4$  eV<sup>137–139</sup>). Since MoS<sub>2</sub> flakes film has been previously reported as HTL,<sup>64,72,94–99</sup> the holes can be extracted from the MAPbI<sub>3</sub> by injecting electrons<sup>145–147</sup> from intergap states of MoS<sub>2</sub>.<sup>152,153</sup> The latter have been reported to be a consequence of the intrinsic presence in MoS<sub>2</sub> of S-vacancies,<sup>153–158</sup> impurities,<sup>159,160</sup> and defects.<sup>161–164</sup> The presence of these intergap states is confirmed by UPS data, which reveal an intrinsic n-type doping of MoS<sub>2</sub> flakes ( $E_F$  is just 0.3 eV inferior to the energy of the energy minimum of the CB and 1.1 eV superior to the energy maximum of the VB). This observation is also in agreement with previous studies,<sup>148–151</sup> which evidenced n-type-doping transport measurements in MoS<sub>2</sub>-based field effect transistors.<sup>148–151</sup> Since XPS analysis revealed equal stoichiometry between MoS<sub>2</sub> flakes and MoS<sub>2</sub> QDs, the hole-extraction mechanism deduced for MoS<sub>2</sub> flakes can also be valid for MoS<sub>2</sub> QDs.<sup>144</sup> We also point out that a similar hole-extraction mechanism has been reported for a MoO<sub>3</sub> anodic interlayer,<sup>146,147,228</sup> due to inherent n-type behavior that allows the material to act as donors in transparent conducting oxides.<sup>229</sup>

**Perovskite Solar Cell Architecture and Their Characterization.** The optoelectronic characterization of MoS<sub>2</sub> QDs evidenced that they hold both hole-extraction and electron-blocking properties, which are the most important requirements for a HTL.<sup>41,40,230</sup> In order to deposit continuous and homogeneous films based on MoS<sub>2</sub> QDs, the latter were hybridized with f-RGO flakes, whose 2D nature spontaneously plugs the pinholes in MoS<sub>2</sub> QD films. With the aim to prove the effectiveness of MoS<sub>2</sub> QDs or MoS<sub>2</sub> QDs:f-RGO as HTL materials, both of them were incorporated into mesoscopic MAPbI<sub>3</sub>-based PSCs to be used as HTL or ABL between MAPbI<sub>3</sub> and spiro-OMeTAD. The investigated PSC has the following architecture: FTO/cTiO<sub>2</sub>/mTiO<sub>2</sub>/MAPbI<sub>3</sub>/ABL (MoS<sub>2</sub> QDs or f-RGO or MoS<sub>2</sub> QDs:f-RGO)/spiro-OMeTAD/Au. The ABLs were also tested as HTLs in the absence of spiro-OMeTAD. Additional details of the device fabrication are reported in [Experimental Methods](#). It is important to note that MoS<sub>2</sub> QDs and MoS<sub>2</sub> QDs:f-RGO nanometer-thick films were deposited onto MAPbI<sub>3</sub> films by spray coating the corresponding dispersions in IPA. The compatibility of the IPA with the MAPbI<sub>3</sub> layer was assessed in

previous experiments.<sup>64,231</sup> A representative FTO/cTiO<sub>2</sub>/mTiO<sub>2</sub>/MAPbI<sub>3</sub>/MoS<sub>2</sub> QDs:f-RGO/spiro-OMeTAD/Au architecture was characterized by cross-sectional scanning electron microscopy (SEM) (Figure 4a). The MoS<sub>2</sub> QDs:f-



**Figure 4.** Morphological SEM characterization of PSCs. (a) Cross-sectional SEM image of a representative FTO/cTiO<sub>2</sub>/mTiO<sub>2</sub>/MAPbI<sub>3</sub>/MoS<sub>2</sub> QDs:f-RGO/spiro-OMeTAD/Au architecture. Top-view SEM images of (b) MAPbI<sub>3</sub> surface and (c) MoS<sub>2</sub> QDs:f-RGO film deposited onto a MAPbI<sub>3</sub> layer.

RGO layer is not resolved because of its nanometer-scale thickness. However, top-view SEM analysis (Figure 4b,c) of the MAPbI<sub>3</sub> surface shows that the contrast between different MAPbI<sub>3</sub> grains is reduced after the deposition of an ultrathin layer of MoS<sub>2</sub> QDs:f-RGO. This indicates the presence of a nanometer-thick film of MoS<sub>2</sub> QDs:f-RGO covering MAPbI<sub>3</sub>. In addition, SEM/elemental analysis by energy-dispersive X-ray spectroscopy (EDX) were performed on the different MAPbI<sub>3</sub>-based PSCs (Figure S8), focusing on Pb ( $M$ , 2.34 keV), Mo ( $L\alpha$ , 2.29 keV), and C ( $K\alpha$ , 0.28 keV) peak signals, to evaluate the coverage of the MAPbI<sub>3</sub> surface with MoS<sub>2</sub> QDs and f-RGO. After the deposition of the MoS<sub>2</sub> QDs:f-RGO, a significant increase of the C signal relative to Pb was observed ( $C/(Pb + Mo)$  atomic ratio =  $15 \pm 2$ ) compared to the reference device (without spiro-OMeTAD,  $C/Pb$  atomic ratio =  $2.2 \pm 0.1$ ). This further confirms the coverage of the MAPbI<sub>3</sub> surface by the MoS<sub>2</sub> QDs:f-RGO film. Similar results were also evidenced by using only f-RGO ( $C/Pb$  atomic ratio =  $16 \pm 2$ ).

The capability of MoS<sub>2</sub> QDs-, f-RGO-, and MoS<sub>2</sub> QDs:f-RGO-based ABLs to effectively collect the photogenerated holes was proved by measuring the PV performance of PSCs without spiro-OMeTAD. The current–voltage ( $I$ – $V$ ) characteristics (Figure 5a) show that the best performances are obtained for PSCs adopting MoS<sub>2</sub> QDs:f-RGO as HTL. Such

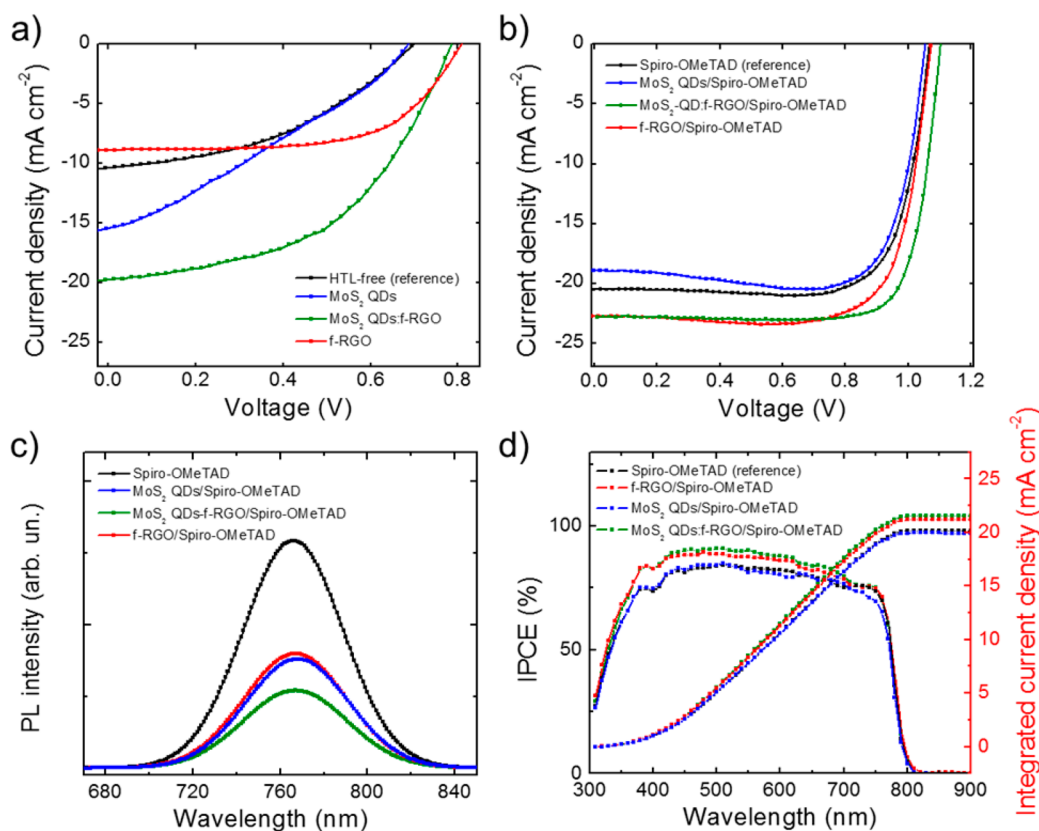


**Figure 5.** (a, b)  $I$ – $V$  characteristics of tested PSCs using MoS<sub>2</sub> QDs, f-RGO, and MoS<sub>2</sub> QDs:f-RGO as HTL (panel a) or ABL between MAPbI<sub>3</sub> and spiro OMeTAD. The data for HTL-free and ABL-free devices are shown as references. (c) Steady-state PL measurements of the MAPbI<sub>3</sub> after deposition of spiro-OMeTAD and ABL/spiro-OMeTAD. (d) Incident power conversion efficiency measurements of the various PSCs. The integrated current density of the curves is also shown on the right y-axis (red color).

PSCs exhibited a significant increase of PCE compared to those without HTL (7.60% vs 3.01%). Also MoS<sub>2</sub> QDs and f-RGO individually enhanced the PV performance of the HTL-free reference. In particular, MoS<sub>2</sub> QDs increased the  $J_{sc}$  of the HTL-free reference from 10.33 mA cm<sup>-2</sup> to 15.52 mA cm<sup>-2</sup>, while f-RGO boosted the  $V_{oc}$  of the HTL-free reference from 0.69 V to 0.81 V. The poor  $V_{oc}$  obtained by the MoS<sub>2</sub> QDs is ascribed to a current leakage in the absence of complete coverage of the MAPbI<sub>3</sub> surface, leading to a charge recombination at the MAPbI<sub>3</sub>/Au interface, since the metallic behavior of Au is not hole-selective.<sup>232,233</sup> This drawback can be overcome by hybridizing MoS<sub>2</sub> QDs with f-RGO, whose planar nature can provide an effective coverage of the MAPbI<sub>3</sub>. These data indicate that the individual components of MoS<sub>2</sub> QDs:f-RGO synergistically improve the PV performance of the cells. Although the measured PV performances are still lower compared to PSC based on conventional HTLs, these results are useful for the development of viable alternative HTLs based on GRMs.

After these preliminary tests, MoS<sub>2</sub> QDs, f-RGO, and MoS<sub>2</sub> QDs:f-RGO were tested as ABLs between MAPbI<sub>3</sub> and spiro-OMeTAD. As shown by the  $I$ – $V$  curves of representative PSCs in Figure 5b, the PV performance increased with the addition of f-RGO and MoS<sub>2</sub> QDs:f-RGO as ABLs compared to the reference device. The “champion cell” using MoS<sub>2</sub> QDs:f-RGO reached a maximum PCE of 20.12%, a  $V_{oc}$  of 1.11 V, a  $J_{sc}$  of 22.81 mA cm<sup>-2</sup>, and an FF of 79.75%. The reference device showed a PCE of 16.85%, with a  $V_{oc}$  1.07 V, a  $J_{sc}$  of 20.28 mA cm<sup>-2</sup>, and an FF of 76.9%. The device using only the MoS<sub>2</sub>

QDs as ABL reached a PCE of only 14.40%, thus without improving the PV performance of the reference one. The incorporation of f-RGO remarkably increases the  $J_{sc}$  of the reference device up to 22.76 mA cm<sup>-2</sup>, reaching a PCE of 18.64%. The enhanced  $J_{sc}$  of the PSCs exploiting f-RGO and MoS<sub>2</sub> QDs:f-RGO compared to the value obtained by both the reference device and the one based on MoS<sub>2</sub> QDs as ABL is attributed to the efficient charge collection in the presence of f-RGO and MoS<sub>2</sub> QDs:f-RGO, respectively. Notably, the optical absorption of the MoS<sub>2</sub> QDs:f-RGO-based PSCs does not show significant differences compared to that of the MoS<sub>2</sub> QDs-based PSC, showing an increase of only ~3% and ~8% compared to f-RGO-based and reference PSCs, respectively (Figure S9). Hysteresis phenomena, such as anomalous dependence on the voltage scan direction/rate/range,<sup>43,234</sup> voltage conditioning history,<sup>235</sup> and device configuration,<sup>36</sup> could affect the  $I$ – $V$  measurements.<sup>236,237</sup> In order to exclude such effects, the PCE over time at the maximum power point was measured for a different batch of cells (Figure S10), confirming that the MoS<sub>2</sub> QDs:f-RGO improves the PSC performance of the reference PSC. Forward and reverse  $I$ – $V$  curves were also collected (see comparative results of the different ABLs tested in the SI, Figure S11), showing that the presence of MoS<sub>2</sub> QDs:f-RGO as ABLs decreases the hysteresis phenomena compared to those of the other investigated PSCs, including the reference device adopting spiro-OMeTAD as HTL without ABL.

Steady-state PL measurements were performed to evaluate the capability of the ABLs to extract the photogenerated holes

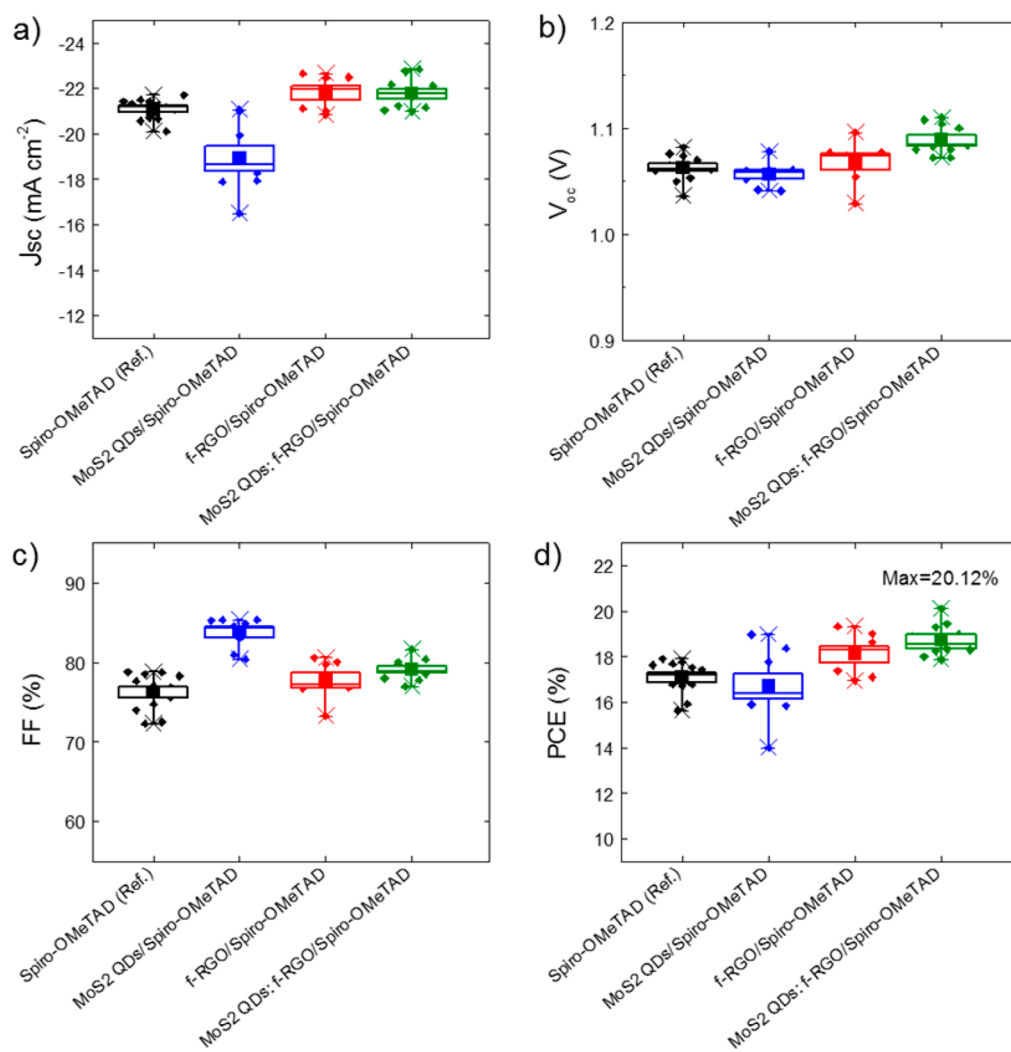


**Figure 6.** Photovoltaic parameters measured at 1 sun with the relative standard deviation on 12 PSCs for the four investigated PSCs using spiro-OMeTAD as HTL and MoS<sub>2</sub> QDs, f-RGO, and MoS<sub>2</sub> QDs:f-RGO as ABLs: (a)  $J_{sc}$ ; (b)  $V_{oc}$ ; (c) FF; and (d) PCE. The average values are indicated by a square (■).

from the MAPbI<sub>3</sub>. In fact, the hole-extraction process hinders the radiative charge recombination in the absorber material,<sup>238–240</sup> which then shows a PL quenching.<sup>241,242</sup> Figure 5c shows that the addition of ABL between MAPbI<sub>3</sub> and spiro-OMeTAD suppressed the PL emission of MAPbI<sub>3</sub>. Quantitatively, the PL decreased by 49.5%, 51.9%, and 65.8% in the presence of f-RGO, MoS<sub>2</sub> QDs, and MoS<sub>2</sub> QDs:f-RGO, respectively. This means that the ABLs can accelerate the hole-extraction dynamics at the photoelectrode.<sup>239,243</sup> However,  $I$ – $V$  measurements clearly show the need of f-RGO to increase the  $J_{sc}$ , indicating that other effects, such as the morphology of the ABL films, practically influence the PV performance of the PSCs. Incident power conversion efficiency (IPCE) measurements (Figure 5d) are consistent with the  $I$ – $V$  ones. In fact, they show that f-RGO and MoS<sub>2</sub> QDs:f-RGO increased the IPCE in the 350–750 nm range by ~5% and ~7% compared to that of the reference device and the MoS<sub>2</sub> QDs-based PSCs, respectively. The trend of integrated current density ( $J_{IPCE}$ ) values calculated from IPCE data in the 300–850 nm range at AM1.5G condition ( $J_{IPCE}(\text{MoS}_2 \text{ QDs:f-RGO}) > J_{IPCE}(\text{f-RGO}) > J_{IPCE}(\text{ref}) > J_{IPCE}(\text{MoS}_2 \text{ QDs})$ ) is in agreement with the  $J_{sc}$  of the different PSCs extrapolated by the corresponding  $I$ – $V$  curves. The improvement of  $V_{oc}$  and FF compared to the PSCs

without spiro-OMeTAD is attributed to both the high WF values of the spiro-OMeTAD compared to those of ABLs, which assist the hole extraction, and the suppression of the contact between MAPbI<sub>3</sub> and Au, where charge recombination and/or chemical degradation of MAPbI<sub>3</sub> can occur.<sup>244</sup>

The statistical PV figures of merit (FoM) measured for each set of PSCs using spiro-OMeTAD as HTL and MoS<sub>2</sub> QDs, f-RGO, and MoS<sub>2</sub> QDs:f-RGO as ABLs are reported in Figure 6, in comparison with those obtained for ABL-free PSC (ref). Table 1 summarizes the PV FoM extracted by the  $I$ – $V$  curves of the PSCs shown in Figure 6. These results demonstrate the reproducibility of the PV performance of the PSCs incorporating the ABLs. In particular, PSCs using MoS<sub>2</sub> QDs:f-RGO exhibited an average PCE value of  $18.86 \pm 0.72\%$ , corresponding to an increase of 10.6% compared to the reference device without ABL (average PCE =  $17.08 \pm 0.73\%$ ).

In addition to PCE, the long-term stability of PSCs is crucial for real applications.<sup>245</sup> Although MAPbI<sub>3</sub> revolutionized the worldwide PV research in the last year, it is intrinsically unstable due to its hygroscopicity and tendency to back-convert into its precursors, namely, PbI<sub>2</sub> and MAI, during moisture,<sup>246–250</sup> oxygen,<sup>246–248,251–253</sup> and light illumination<sup>246–248,251,254</sup> exposure. In addition, MAPbI<sub>3</sub> undergoes a

**Table 1.** Photovoltaic FOM Extracted by the  $I$ - $V$  Curves of the Best Performing Device and the Average PCE of Each Type of PSCs Using spiro-OMeTAD as HTL and MoS<sub>2</sub> QDs, f-RGO, and MoS<sub>2</sub> QDs:f-RGO as ABLs

structure of PSC	$V_{oc}$ [V]	$J_{sc}$ [mA cm <sup>-2</sup> ]	FF [%]	PCE [%]	average PCE <sup>a</sup> [%]
spiro-OMeTAD	1.06	21.49	78.31	17.53	17.08 ± 0.73
MoS <sub>2</sub> QDs/spiro-OMeTAD	1.06	20.98	83.02	18.98	16.71 ± 1.60
f-RGO/spiro-OMeTAD	1.07	22.49	80.61	19.34	18.11 ± 0.96
MoS <sub>2</sub> QDs:f-RGO/spiro-OMeTAD	1.11	22.81	79.75	20.12	18.76 ± 0.72

<sup>a</sup>Average PCE on 12 devices for each type of PSC together with the standard error.

phase transition from the tetragonal to cubic phase at ~54 °C,<sup>255–257</sup> a temperature that can be reached during typical solar cell operation, being incompatible with certification requirement of solar modules (–40–85 °C temperature range).<sup>257</sup> This represents the major constraint for the market breakthrough of this technology.<sup>190,258</sup> So far, the chemical engineering of the perovskite absorber elemental composition has been proved to address the instability issues.<sup>25,259,260</sup> A device lifetime close to market requirements, e.g., 500 h stability and >20% PCE, has been recently achieved by formulating perovskites with mixed cations, i.e., formamidinium (FA), MA, and inorganic species (Cs or Ru).<sup>261,262</sup> One-year stable PSCs were achieved by engineering an ultrastable 2D/3D (HOOC(CH<sub>2</sub>)<sub>4</sub>NH<sub>3</sub>)<sub>2</sub>PbI<sub>4</sub>/CH<sub>3</sub>NH<sub>3</sub>PbI<sub>3</sub> perovskite junction.<sup>39</sup> Despite this result, interface engineering of PSCs also affects their stability,<sup>16,60,61,69,263</sup> since the diffusion of elemental species such as iodine(I) and metal from the electrode materials (e.g., Au<sup>244</sup> or Ag<sup>264</sup>) has been recently correlated with the degradation of interfaces and the decay of the PV properties.<sup>265</sup> In this context, the incorporation of graphene flakes into mTiO<sub>2</sub> has been demonstrated to increase the chemical stability of overlying MAPbI<sub>3</sub>, which exhibited higher crystalline quality compared to that of MAPbI<sub>3</sub> deposited directly onto mTiO<sub>2</sub><sup>69</sup> and a frozen tetragonal phase regardless of the temperature.<sup>69</sup> An active buffer layer based on GRMs improved the charge extraction process compared to that of the ABL-free reference, preventing the degradation induced by the diffusion of Au and I.<sup>71,104,231,266,267</sup> Although it was not the goal of our work to overcome the intrinsic instability of MAPbI<sub>3</sub>, the stability of the devices after encapsulation was measured in ISOS-D-1 shelf life aging test protocol<sup>268</sup> (Figure 7). After a 1032 h aging test, the ABL-based PSCs exhibited a decrease of PCE of only 13.5%, 11.2%, and 8.8% for MoS<sub>2</sub> QDs-, f-RGO-, and MoS<sub>2</sub> QDs:f-RGO-based PSCs, respectively. These reduced values are significantly lower than the ones shown by the reference PSC without ABL (24.6%).

The improved stability of the ABL-based PSCs compared to the reference PSC is ascribed to the surface passivation of the perovskite layer provided by the ABLs, which mitigate the I migration from the MAPbI<sub>3</sub> into the spiro-OMeTAD<sup>269</sup> and the formation of Au pathways from the metal electrode to the MAPbI<sub>3</sub>.<sup>270</sup>

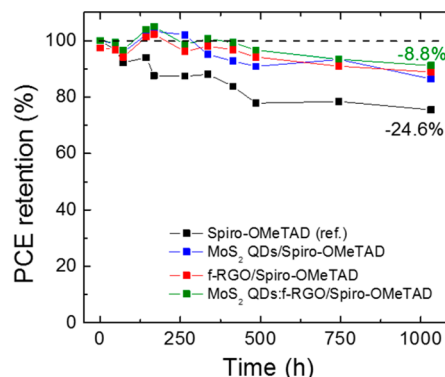


**Figure 7.** Normalized PCE trends vs time extracted by  $I$ - $V$  characteristics under 1 SUN illumination, periodically acquired during the shelf life test (ISOS-D-1) for the four PSCs.

## CONCLUSIONS

In conclusion, solution-processed low-dimensional materials can be designed and combined to improve both efficiency and stability performances of PSCs *via* interface engineering. These results, coupled with the availability of a wide library of 2D materials, demonstrate that GIE is a powerful tool for boosting the PV performance of PSCs. Moreover, 2D materials can be directly produced from cost-effective and environmentally friendly solution-processed methods<sup>78</sup> from their bulk counterparts,<sup>81–84</sup> allowing inks with on-demand (opto)electronic properties to be formulated.<sup>86–88</sup> Solution-processed 2D materials can be deposited on different substrates using established printing/coating techniques,<sup>87</sup> in order to be integrated as functional layers (e.g., charge transport layers and ABLs) into the PSC structures.<sup>271</sup> By a deep exploitation of the potential offered by 2D materials,<sup>75,199</sup> we “*ad-hoc*” designed MoS<sub>2</sub> QDs anchored to the functional site of RGO flakes to effectively collect the photogenerated holes (as well as to block electrons) from MAPbI<sub>3</sub> toward the anode contact in mesoscopic architecture, reaching a maximum PCE value of 20.12% (average PCE of 18.8%). The use of 2D materials is also beneficial for the stability increase of mesoscopic, indicating the feasibility toward next-generation PSCs, which exploit both GIE and efficient and stable perovskite chemistries, including mixed cation/halide and 2D perovskites.

## EXPERIMENTAL METHODS

**Production of Materials.** Graphene oxide was synthesized from graphite flakes (Sigma-Aldrich, +100 mesh ≥75% min) using a modified Hummer’s method.<sup>182</sup> Briefly, 1 g of graphite and 0.5 g of NaNO<sub>3</sub> (Sigma-Aldrich, reagent grade) were mixed, followed by the dropwise addition of 25 mL of H<sub>2</sub>SO<sub>4</sub> (Sigma-Aldrich). After 4 h, 3 g of KMnO<sub>4</sub> (Alpha Aesar, ACS 99%) was added slowly to the above solution, keeping the temperature at 4 °C with the aid of an ice bath. The mixture was let to react at room temperature overnight, and the resulting solution was diluted by adding 2 L of distilled water under vigorous stirring. The sample was filtered and rinsed with H<sub>2</sub>O. Finally the sample was dried at 110 °C overnight.

Reduced graphene oxide was produced by thermal reduction of the as-produced GO<sup>180,181</sup> in a quartz tube (120 cm length and 25 mm inner diameter) passing through a three-zone split furnace (PSC 12/--/600H, Lenton, UK). Experimentally, gas flows were controlled upstream by an array of mass flow controllers (1479A, mks, USA). Under a 100 sccm flow of Ar/H<sub>2</sub> (90/10%), 100 mg of GO was heated to 100 °C for 20 min to remove the presence of water residuals. Subsequently, a ramp of 20 °C min<sup>-1</sup> was used to reach

1000 °C and stabilized at this temperature for 2 h. Finally, the oven was left to cool to room temperature.

The RGO was functionalized with MPTS (95%, Sigma-Aldrich) in an ethanol (absolute alcohol,  $\geq 99.8\%$ , without additive, Sigma-Aldrich) solution by reflux at 60 °C for 15 h.<sup>166</sup> For this reaction 250  $\mu\text{L}$  of MPTS was added per mg of RGO. After the synthesis, the silane-functionalized RGO material was recovered by centrifugation (9000 rpm) and redispersed in ethanol (EtOH) by vortexing for a second centrifugation (9000 rpm) to remove unreacted silane. A solvent-exchange process<sup>184,185,95</sup> was carried out to redisperse the f-RGO in IPA at a concentration of 0.4 mg mL<sup>-1</sup>.

Molybdenum disulfide quantum dots were produced through a one-step solvothermal method starting from MoS<sub>2</sub> flakes, produced by LPE<sup>144</sup> of bulk MoS<sub>2</sub> crystals in IPA followed by SBS.<sup>172,173</sup> In detail, 30 mg of MoS<sub>2</sub> bulk crystal (Sigma-Aldrich) was added to 50 mL of IPA and then ultrasonicated (Branson 5800 cleaner, Branson Ultrasonics) for 8 h. The resulting dispersion was ultracentrifuged (Optima XE-90 ultracentrifuge, Beckman Coulter) for 15 min at 2700g, in order to separate the unexfoliated MoS<sub>2</sub> crystals (collected as sediment) from the thinner MoS<sub>2</sub> flakes that remain in the supernatant. Then, the sample was refluxed in air under stirring for 24 h at 140 °C. The resulting dispersion was subsequently ultracentrifuged for 30 min at 24600g. Afterward, the supernatant was collected, obtaining the MoS<sub>2</sub> QDs dispersion. By evaporating the solvent, a concentration of 0.2 mg mL<sup>-1</sup> was obtained.

The hybrid dispersion between MoS<sub>2</sub> QDs and f-RGO was produced by mixing the as-produced component dispersions in a volume ratio of 1:1 (corresponding to a weight ratio of 1:2). By evaporating the solvent, the concentration was doubled in order to have the same amount of the material compared to the native dispersions.

**Characterization of Materials.** Transmission electron microscopy images were taken with a JEM 1011 (JEOL) TEM (thermionic W filament), operating at 100 kV. Morphological and statistical analysis was carried out by using ImageJ software (NIH) and OriginPro 9.1 software (OriginLab), respectively. The statistical analysis was performed on 50 flakes from the different TEM images collected. The lateral dimension of each flake was calculated as the maximum Feret's diameter. Samples for the TEM measurements were prepared by drop casting the material dispersions onto ultrathin carbon-coated copper grids rinsed with deionized water and subsequently dried under vacuum overnight.

Atomic force microscopy images were taken using a Nanowizard III (JPK Instruments, Germany) mounted onto an Axio Observer D1 (Carl Zeiss, Germany) inverted optical microscope. The AFM measurements were carried out by using PPP-NCHR cantilevers (Nanosensors, USA) with a nominal tip diameter of 10 nm. A drive frequency of  $\sim 295$  kHz was used. Intermittent contact mode AFM images ( $512 \times 512$  data points) of  $2.5 \times 2.5 \mu\text{m}^2$  were collected by keeping the working set point above 70% of the free oscillation amplitude. The scan rate for acquisition of images was 0.7 Hz. Height profiles were processed by using the JPK Data Processing software (JPK Instruments, Germany), and the data were analyzed with OriginPro 9.1 software. Statistical analysis was carried out by means of Origin 9.1 software on multiple AFM images for each sample and calculated on 50 flakes. The samples were prepared by drop-casting the material dispersions onto mica sheets (G250-1, Agar Scientific Ltd., Essex, U.K.) and dried under vacuum.

Optical absorption spectroscopy measurements were carried out on material dispersions by using a Cary Varian 5000 UV–vis spectrometer.

X-ray photoelectron spectroscopy characterization was carried out on a Kratos Axis UltraDLD spectrometer, using a monochromatic Al K $\alpha$  source (15 kV, 20 mA). The spectra were taken on a  $300 \times 700 \mu\text{m}^2$  area. Wide scans were collected with a constant pass energy of 160 eV and an energy step of 1 eV. High-resolution spectra were acquired at a constant pass energy of 10 eV and energy step of 0.1 eV. The binding energy scale was referenced to the C 1s peak at 284.8 eV. The spectra were analyzed using the CasaXPS software (version 2.3.17). The samples were prepared by drop-casting the material

dispersions onto a Si/SiO<sub>2</sub> substrate (LDB Technologies Ltd.) and dried under vacuum.

Fourier-transform infrared spectroscopy was performed in a Bruker Vertex 70v (4000–400 cm<sup>-1</sup> range, 100 scans). The samples were prepared by drop casting MPTS, RGO, f-RGO, and MoS<sub>2</sub> QDs:f-RGO films on BaF<sub>2</sub> substrates (IR grade, Crystran, IR open window 4000 to 600 cm<sup>-1</sup>).

Ultraviolet photoelectron spectroscopy analysis was performed to estimate the Fermi energy level ( $E_F$ ) of the materials under investigation with the same equipment used for XPS and adopting a He I (21.22 eV) discharge lamp. The  $E_F$  was measured from the threshold energy for the emission of secondary electrons during He I excitation. A  $-9.0$  V bias was applied to the sample in order to precisely determine the low kinetic energy cutoff. The samples were prepared by drop casting onto 50 nm Au-sputter-coated silicon wafers.

**Fabrication of Solar Cells.** The solar cells containing four devices were fabricated on laser-patterned glass/FTO substrates (Pilkington,  $8 \Omega \square^{-1}$ ), which were washed for 15 min with acetone, ethanol, and deionized water in an ultrasonic bath, respectively. Furthermore, a compact 40 nm TiO<sub>2</sub> layer (c-TiO<sub>2</sub>) was deposited onto the precleaned laser-patterned FTO glass *via* spray pyrolysis (450 °C) from a solution consisting of 0.16 M diisopropoxytitanium bis(acetylacetonate) (Ti(AcAc)<sub>2</sub>) and 0.4 M acetyl acetone (AcAc) in ethanol. For the mesoporous TiO<sub>2</sub> (m-TiO<sub>2</sub>) layer, anatase TiO<sub>2</sub> nanoparticle paste (30NRD, GreatCell SolarDyesol) was dissolved in ethanol by stirring at a w/w ratio of 1:6. A mesoporous layer was deposited onto c-TiO<sub>2</sub> by spin-coating 140  $\mu\text{L}$  of paste at 3000 rpm for 15 s and subsequently sintered at 480 °C for 30 min.

Successively, a MAPbI<sub>3</sub> perovskite absorber layer was deposited by a solvent engineering method. Briefly 717.76 mg mL<sup>-1</sup> of PbI<sub>2</sub> and 247.56 mg mL<sup>-1</sup> of CH<sub>3</sub>NH<sub>3</sub>I were dissolved in DMF/DMSO (8:1, v/v) by stirring for 24 h at room temperature to obtain the perovskite-based solution. A 70  $\mu\text{L}$  amount of the perovskite solution was spin coated on the mesoporous layer with two-step spinning, first 1000 rpm for 10 s and then 5000 rpm for 45 s. Just 34 s before the end of the second spin-coating step, 0.7 mL of diethyl ether was dropped on the substrates. Subsequently, the perovskite layer was treated with a double-step annealing process, performed at 50 °C for 2 min and then at 100 °C for 10 min. After the heat treatment of the perovskite layer, the 2D materials dispersed in IPA were deposited by automated spray-coating equipment (Aurel) onto the perovskite layer by using N<sub>2</sub> flow (see SI, for the spray parameter settings, Figure S12). A 100  $\mu\text{L}$  amount of the HTL material solution containing spiro-OMeTAD (73.5 mg mL<sup>-1</sup>, Borun sublimed grade  $>99.8\%$ ) in chlorobenzene (Sigma-Aldrich) doped with 26  $\mu\text{L}$  of *tert*-butylpyridine (TBP, Sigma-Aldrich, 96%), 16.6  $\mu\text{L}$  of lithium bis(trifluoromethanesulfonyl)imide (Li-TFSI, Sigma-Aldrich, 99.95%) of stock solution (520 mg in 1 mL acetonitrile, Sigma-Aldrich), and 7.2  $\mu\text{L}$  of cobalt(III) complex solution (FK209 from Lumtec) was deposited by spin coating at 2000 rpm for 20 s. Finally, 80 nm of Au counter electrode was deposited by thermal evaporation in high-vacuum conditions ( $10^{-6}$  mbar). For the shelf life tests, the device were encapsulated following the protocol previously reported in ref 269.

**Characterization of Solar Cells.** Scanning electron microscopy analysis of solar cells was performed using a Helios Nanolab 600 DualBeam microscope (FEI Company) and 10 kV and 0.2 nA as measurement conditions. For the EDX spectra acquisition and analysis on the solar cells we used the microscope combined with an X-Max detector and INCA system (Oxford Instruments) and 15 kV and 0.8 nA as measurement conditions. The samples were imaged without any metal coating or pretreatment. To evaluate the layered stack of the solar cell by cross section, the samples were prepared using focused ion beam coupled to the microscope.

Current–voltage characteristics of masked and encapsulated devices were acquired in air atmosphere by using a solar simulator (ABET Sun 2000, class A) at AM1.5 and 100 mW cm<sup>-2</sup> illumination conditions, calibrated with a certified reference Si cell (RERA Solutions RR-1002). Devices were not preconditioned before the  $I$ – $V$  measurements.  $I$ – $V$  scans were performed by using a scan rate of 20

mV s<sup>-1</sup>. Incident photon to current conversion efficiency spectra acquisition was carried out by means of a homemade setup composed by a monochromator (Newport, model 74000) coupled with a Xe lamp (Oriel Apex, Newport) and a source meter (Keithley, model 2612). A homemade LabVIEW program controlled the spectra acquisition.

Shelf life test was carried out on encapsulated devices (by following the indications of the ISOS-D-1 shelf life aging test protocol).<sup>272</sup> In particular, the devices were kept in dark, dry conditions (relative humidity <50%) and at open circuit.

## ASSOCIATED CONTENT

### Supporting Information

The Supporting Information is available free of charge on the ACS Publications website at DOI: 10.1021/acsnano.8b05514.

Supplementary TEM, AFM measurements of MoS<sub>2</sub> and RGO flakes; gravitational sedimentation study of the RGO and f-RGO dispersion in EtOH; PL measurement of MoS<sub>2</sub> QDs; supplementary Tauc analysis of MoS<sub>2</sub> QDs; SEM/EDX measurements of the MAPbI<sub>3</sub>/MoS<sub>2</sub> QDs:f-RGO; optical absorption spectroscopy measurements of PSCs; stabilized PCE measurements; spray coating parameter optimization for MoS<sub>2</sub> QDs, f-RGO, and MoS<sub>2</sub> QDs:f-RGO film deposition (PDF)

## AUTHOR INFORMATION

### Corresponding Authors

\*Tel: +39 0672597456. E-mail: aldo.dicarlo@uniroma2.it.

\*Tel: +39 01071781795. E-mail: francesco.bonaccorso@iit.it.

### ORCID

Reinier Oropesa-Nuñez: 0000-0002-9551-6565

Mirko Prato: 0000-0002-2188-8059

Antonio E. Del Rio Castillo: 0000-0001-9678-1187

Aldo Di Carlo: 0000-0001-6828-2380

Francesco Bonaccorso: 0000-0001-7238-9420

### Author Contributions

#L. Najafi and B. Taheri contributed equally.

### Funding

This project has received funding from the European Union's Horizon 2020 Research and Innovation Program under grant agreement no.785219-GrapheneCore2.

### Notes

The authors declare no competing financial interest.

## ACKNOWLEDGMENTS

We thank Electron Microscopy Facility—Istituto Italiano di Tecnologia for support in TEM data acquisition and IIT Clean Room Facility and Smart Materials Group for the access to carry out SEM/EDS measurements and FTIR characterization, respectively. A.D.C. gratefully acknowledges the financial support of the Ministry of Education and Science of the Russian Federation in the framework of Megagrant No. 14.Y26.31.0027.

## REFERENCES

- (1) Green, M. A.; Ho-Baillie, A.; Snaith, H. J. The Emergence of Perovskite Solar Cells. *Nat. Photonics* **2014**, *8*, 506.
- (2) Park, N.-G. Perovskite Solar Cells: An Emerging Photovoltaic Technology. *Mater. Today* **2015**, *18*, 65–72.
- (3) Grätzel, M. The Light and Shade of Perovskite Solar Cells. *Nat. Mater.* **2014**, *13*, 838.

- (4) Stranks, S. D.; Snaith, H. J. Metal-Halide Perovskites for Photovoltaic and Light-Emitting Devices. *Nat. Nanotechnol.* **2015**, *10*, 391.

- (5) Green, M. The Path to 25% Silicon Solar Cell Efficiency: History of Silicon Cell Evolution. *Prog. Photovoltaics* **2009**, *17*, 183–189.

- (6) Masuko, K.; Shigematsu, M.; Hashiguchi, T.; Fujishima, D.; Kai, M.; Yoshimura, N.; Yamaguchi, T.; Ichihashi, Y.; Mishima, T.; Matsubara, N.; Yamanishi, T. Achievement of More Than 25% Conversion Efficiency With Crystalline Silicon Heterojunction Solar Cell. *IEEE J. Photovolt.* **2014**, *4*, 1433–1435.

- (7) Yoshikawa, K.; Kawasaki, H.; Yoshida, W.; Irie, T.; Konishi, K.; Nakano, K.; Uto, T.; Adachi, D.; Kanematsu, M.; Uzu, H.; Yamamoto, K. Silicon Heterojunction Solar Cell with Interdigitated Back Contacts for a Photoconversion Efficiency over 26%. *Nat. Energy* **2017**, *2*, 17032.

- (8) Lee, T. D.; Ebong, A. U. A Review of Thin Film Solar Cell Technologies and Challenges. *Renewable Sustainable Energy Rev.* **2017**, *70*, 1286–1297.

- (9) Shah, A.; Torres, P.; Tscharnner, R.; Wyrsh, N.; Keppner, H. Photovoltaic Technology: The Case for Thin-Film Solar Cells. *Science* **1999**, *285*, 692–698.

- (10) (NREL), T. N. C. for P. (NCPV) at the N. R. E. L. Best Research-Cell Efficiency available from: <https://www.nrel.gov/pv/assets/pdfs/pv-efficiencies-07-17-2018.pdf> (accessed on 05/09/2018).

- (11) Green, M. A.; Ho-Baillie, A. Perovskite Solar Cells: The Birth of a New Era in Photovoltaics. *ACS Energy Lett.* **2017**, *2*, 822–830.

- (12) Chuantian, Z.; Bolink, H.; Hongwei, H.; Jinsong, H.; David, C.; Liming, D. Advances in Perovskite Solar Cells. *Adv. Sci.* **2016**, *3*, 1500324.

- (13) Snaith, H. J. Perovskites: The Emergence of a New Era for Low-Cost, High-Efficiency Solar Cells. *J. Phys. Chem. Lett.* **2013**, *4*, 3623–3630.

- (14) Jeon, N. J.; Noh, J. H.; Kim, Y. C.; Yang, W. S.; Ryu, S.; Seok, S. I. Solvent Engineering for High-Performance Inorganic–organic Hybrid Perovskite Solar Cells. *Nat. Mater.* **2014**, *13*, 897.

- (15) Nie, W.; Tsai, H.; Asadpour, R.; Blancon, J.-C.; Neukirch, A. J.; Gupta, G.; Crochet, J. J.; Chhowalla, M.; Tretiak, S.; Alam, M. A.; Wang, H. L. High-Efficiency Solution-Processed Perovskite Solar Cells with Millimeter-Scale Grains. *Science* **2015**, *347*, 522–525.

- (16) Chen, W.; Wu, Y.; Yue, Y.; Liu, J.; Zhang, W.; Yang, X.; Chen, H.; Bi, E.; Ashraful, I.; Grätzel, M.; Han, L. Efficient and Stable Large-Area Perovskite Solar Cells with Inorganic Charge Extraction Layers. *Science* **2015**, *350*, 944–948.

- (17) Li, X.; Bi, D.; Yi, C.; Decoppet, J.-D.; Luo, J.; Zakeeruddin, S. M.; Hagfeldt, A.; Grätzel, M. A Vacuum Flash-Assisted Solution Process for High-Efficiency Large-Area Perovskite Solar Cells. *Science* **2016**, *353*, 58–62.

- (18) Priyadarshi, A.; Haur, L. J.; Murray, P.; Fu, D.; Kulkarni, S.; Xing, G.; Sum, T. C.; Mathews, N.; Mhaisalkar, S. G. A Large Area (70 cm<sup>2</sup>) Monolithic Perovskite Solar Module with a High Efficiency and Stability. *Energy Environ. Sci.* **2016**, *9*, 3687–3692.

- (19) Hwang, K.; Jung, Y.-S.; Heo, Y.-J.; Scholes, F. H.; Watkins, S. E.; Subbiah, J.; Jones, D. J.; Kim, D.-Y.; Vak, D. Toward Large Scale Roll-to-Roll Production of Fully Printed Perovskite Solar Cells. *Adv. Mater.* **2015**, *27*, 1241–1247.

- (20) Lee, M. M.; Teuscher, J.; Miyasaka, T.; Murakami, T. N.; Snaith, H. J. Efficient Hybrid Solar Cells Based on Meso-Superstructured Organometal Halide Perovskites. *Science* **2012**, *338*, 643–647.

- (21) Kojima, A.; Teshima, K.; Shirai, Y.; Miyasaka, T. Organometal Halide Perovskites as Visible-Light Sensitizers for Photovoltaic Cells. *J. Am. Chem. Soc.* **2009**, *131*, 6050–6051.

- (22) Im, J.-H.; Lee, C.-R.; Lee, J.-W.; Park, S.-W.; Park, N.-G. 6.5% Efficient Perovskite Quantum-Dot-Sensitized Solar Cell. *Nanoscale* **2011**, *3*, 4088–4093.

- (23) Yang, W. S.; Noh, J. H.; Jeon, N. J.; Kim, Y. C.; Ryu, S.; Seo, J.; Seok, S. I. High-Performance Photovoltaic Perovskite Layers

Fabricated through Intramolecular Exchange. *Science* **2015**, *348*, 1234–1237.

(24) Ansari, M. I. H.; Qurashi, A.; Nazeeruddin, M. K. Frontiers, Opportunities, and Challenges in Perovskite Solar Cells: A Critical Review. *J. Photochem. Photobiol., C* **2018**, *35*, 1–24.

(25) Ono, L. K.; Juarez-Perez, E. J.; Qi, Y. Progress on Perovskite Materials and Solar Cells with Mixed Cations and Halide Anions. *ACS Appl. Mater. Interfaces* **2017**, *9*, 30197–30246.

(26) Yang, W. S.; Park, B.-W.; Jung, E. H.; Jeon, N. J.; Kim, Y. C.; Lee, D. U.; Shin, S. S.; Seo, J.; Kim, E. K.; Noh, J. H.; Seok, S. I. Iodide Management in Formamidinium-Lead-Halide-based Perovskite Layers for Efficient Solar Cells. *Science* **2017**, *356*, 1376–1379.

(27) Zhou, H.; Chen, Q.; Li, G.; Luo, S.; Song, T.; Duan, H.-S.; Hong, Z.; You, J.; Liu, Y.; Yang, Y. Interface Engineering of Highly Efficient Perovskite Solar Cells. *Science* **2014**, *345*, 542–546.

(28) Yang, G.; Chen, C.; Yao, F.; Chen, Z.; Zhang, Q.; Zheng, X.; Ma, J.; Lei, H.; Qin, P.; Xiong, L.; Ke, W. Effective Carrier-Concentration Tuning of SnO<sub>2</sub> Quantum Dot Electron-Selective Layers for High-Performance Planar Perovskite Solar Cells. *Adv. Mater.* **2018**, *30*, 1706023.

(29) Xie, J.; Huang, K.; Yu, X.; Yang, Z.; Xiao, K.; Qiang, Y.; Zhu, X.; Xu, L.; Wang, P.; Cui, C.; Yang, D. Enhanced Electronic Properties of SnO<sub>2</sub> via Electron Transfer from Graphene Quantum Dots for Efficient Perovskite Solar Cells. *ACS Nano* **2017**, *11*, 9176–9182.

(30) Zhao, J.; Zheng, X.; Deng, Y.; Li, T.; Shao, Y.; Gruverman, A.; Shield, J.; Huang, J. Is Cu a Stable Electrode Material in Hybrid Perovskite Solar Cells for a 30-Year Lifetime? *Energy Environ. Sci.* **2016**, *9*, 3650–3656.

(31) Shin, S. S.; Yeom, E. J.; Yang, W. S.; Hur, S.; Kim, M. G.; Im, J.; Seo, J.; Noh, J. H.; Seok, S. I. Colloidally Prepared La-Doped BaSnO<sub>3</sub> Electrodes for Efficient, Photostable Perovskite Solar Cells. *Science* **2017**, *356*, 167–171.

(32) Jun-Yuan, J.; Yi-Fang, C.; Mu-Huan, L.; Shin-Rung, P.; Tzung-Fang, G.; Peter, C.; Ten-Chin, W. CH<sub>3</sub>NH<sub>3</sub>PbI<sub>3</sub> Perovskite/Fullerene Planar-Heterojunction Hybrid Solar Cells. *Adv. Mater.* **2013**, *25*, 3727–3732.

(33) Kim, H.-S.; Park, N.-G. Parameters Affecting I–V Hysteresis of CH<sub>3</sub>NH<sub>3</sub>PbI<sub>3</sub> Perovskite Solar Cells: Effects of Perovskite Crystal Size and Mesoporous TiO<sub>2</sub> Layer. *J. Phys. Chem. Lett.* **2014**, *5*, 2927–2934.

(34) Bi, D.; Yang, L.; Boschloo, G.; Hagfeldt, A.; Johansson, E. M. J. Effect of Different Hole Transport Materials on Recombination in CH<sub>3</sub>NH<sub>3</sub>PbI<sub>3</sub> Perovskite-Sensitized Mesoscopic Solar Cells. *J. Phys. Chem. Lett.* **2013**, *4*, 1532–1536.

(35) Zhao, P.; Kim, B. J.; Jung, H. S. Passivation in Perovskite Solar Cells: A Review. *Mater. Today Energy* **2018**, *7*, 267–286.

(36) Shao, Y.; Xiao, Z.; Bi, C.; Yuan, Y.; Huang, J. Origin and Elimination of Photocurrent Hysteresis by Fullerene Passivation in CH<sub>3</sub>NH<sub>3</sub>PbI<sub>3</sub> Planar Heterojunction Solar Cells. *Nat. Commun.* **2014**, *5*, 5784.

(37) Xing, G.; Mathews, N.; Sun, S.; Lim, S. S.; Lam, Y. M.; Grätzel, M.; Mhaisalkar, S.; Sum, T. C. Long-Range Balanced Electron- and Hole-Transport Lengths in Organic-Inorganic CH<sub>3</sub>NH<sub>3</sub>PbI<sub>3</sub>. *Science* **2013**, *342*, 344–347.

(38) Yang, G.; Wang, C.; Lei, H.; Zheng, X.; Qin, P.; Xiong, L.; Zhao, X.; Yan, Y.; Fang, G. Interface Engineering in Planar Perovskite Solar Cells: Energy Level Alignment, Perovskite Morphology Control and High Performance Achievement. *J. Mater. Chem. A* **2017**, *5*, 1658–1666.

(39) Grancini, G.; Roldán-Carmona, C.; Zimmermann, I.; Mosconi, E.; Lee, X.; Martineau, D.; Narbey, S.; Oswald, F.; De Angelis, F.; Graetzel, M.; Nazeeruddin, M. K. One-Year Stable Perovskite Solar Cells by 2D/3D Interface Engineering. *Nat. Commun.* **2017**, *8*, 15684.

(40) Malinkiewicz, O.; Yella, A.; Lee, Y. H.; Espallargas, G. M.; Graetzel, M.; Nazeeruddin, M. K.; Bolink, H. J. Perovskite Solar Cells Employing Organic Charge-Transport Layers. *Nat. Photonics* **2014**, *8*, 128.

(41) Grill, I.; Aygüler, M. F.; Bein, T.; Docampo, P.; Hartmann, N. F.; Handloser, M.; Hartschuh, A. Charge Transport Limitations in Perovskite Solar Cells: The Effect of Charge Extraction Layers. *ACS Appl. Mater. Interfaces* **2017**, *9*, 37655–37661.

(42) Snaith, H. J.; Abate, A.; Ball, J. M.; Eperon, G. E.; Leijtens, T.; Noel, N. K.; Stranks, S. D.; Wang, J. T.-W.; Wojciechowski, K.; Zhang, W. Anomalous Hysteresis in Perovskite Solar Cells. *J. Phys. Chem. Lett.* **2014**, *5*, 1511–1515.

(43) Unger, E. L.; Hoke, E. T.; Bailie, C. D.; Nguyen, W. H.; Bowring, A. R.; Heumüller, T.; Christoforo, M. G.; McGehee, M. D. Hysteresis and Transient Behavior in Current-Voltage Measurements of Hybrid-Perovskite Absorber Solar Cells. *Energy Environ. Sci.* **2014**, *7*, 3690–3698.

(44) Heo, J. H.; Han, H. J.; Kim, D.; Ahn, T. K.; Im, S. H. Hysteresis-Less Inverted CH<sub>3</sub>NH<sub>3</sub>PbI<sub>3</sub> Planar Perovskite Hybrid Solar Cells with 18.1% Power Conversion Efficiency. *Energy Environ. Sci.* **2015**, *8*, 1602–1608.

(45) Pascoe, A. R.; Yang, M.; Kopidakis, N.; Zhu, K.; Reese, M. O.; Rumbles, G.; Fekete, M.; Duffy, N. W.; Cheng, Y.-B. Planar versus Mesoscopic Perovskite Microstructures: The Influence of CH<sub>3</sub>NH<sub>3</sub>PbI<sub>3</sub> Morphology on Charge Transport and Recombination Dynamics. *Nano Energy* **2016**, *22*, 439–452.

(46) Yang, B.; Xiangyue, M.; Shihe, Y. Interface Engineering for Highly Efficient and Stable Planar P-I-N Perovskite Solar Cells. *Adv. Energy Mater.* **2018**, *8*, 1701883.

(47) Schulz, P.; Edri, E.; Kirmayer, S.; Hodes, G.; Cahen, D.; Kahn, A. Interface Energetics in Organo-Metal Halide Perovskite-Based Photovoltaic Cells. *Energy Environ. Sci.* **2014**, *7*, 1377–1381.

(48) Sum, T. C.; Chen, S.; Xing, G.; Liu, X.; Wu, B. Energetics and Dynamics in Organic–inorganic Halide Perovskite Photovoltaics and Light Emitters. *Nanotechnology* **2015**, *26*, 342001.

(49) Azhar, F.; Lukas, S.-M.; Germà, G.-B.; Rajan, J.; Ivan, M.-S. Interfaces in Perovskite Solar Cells. *Adv. Energy Mater.* **2017**, *7* (22), 1700623.

(50) Schulz, P. Interface Design for Metal Halide Perovskite Solar Cells. *ACS Energy Lett.* **2018**, *3*, 1287–1293.

(51) Sherkar, T. S.; Momblona, C.; Gil-Escrig, L.; Ávila, J.; Sessolo, M.; Bolink, H. J.; Koster, L. J. A. Recombination in Perovskite Solar Cells: Significance of Grain Boundaries, Interface Traps, and Defect Ions. *ACS Energy Lett.* **2017**, *2*, 1214–1222.

(52) Pantaler, M.; Cho, K. T.; Queloz, V. I. E.; García Benito, I.; Fettkenhauer, C.; Anusca, I.; Nazeeruddin, M. K.; Lupascu, D. C.; Grancini, G. Hysteresis-Free Lead-Free Double-Perovskite Solar Cells by Interface Engineering. *ACS Energy Lett.* **2018**, *3*, 1781–1786.

(53) Peng, J.; Wu, Y.; Ye, W.; Jacobs, D. A.; Shen, H.; Fu, X.; Wan, Y.; Duong, T.; Wu, N.; Barugkin, C.; Nguyen, H. T.; Zhong, D. Interface Passivation Using Ultrathin Polymer–fullerene Films for High-Efficiency Perovskite Solar Cells with Negligible Hysteresis. *Energy Environ. Sci.* **2017**, *10*, 1792–1800.

(54) Lira-Cantú, M. Perovskite Solar Cells: Stability Lies at Interfaces. *Nat. Energy* **2017**, *2*, 17115.

(55) Christians, J. A.; Schulz, P.; Tinkham, J. S.; Schloemer, T. H.; Harvey, S. P.; Tremolet de Villers, B. J.; Sellinger, A.; Berry, J. J.; Luther, J. M. Tailored Interfaces of Unencapsulated Perovskite Solar Cells for > 1,000 h Operational Stability. *Nat. Energy* **2018**, *3*, 68–74.

(56) Sha, W. E. I.; Ren, X.; Chen, L.; Choy, W. C. H. The Efficiency Limit of CH<sub>3</sub>NH<sub>3</sub>PbI<sub>3</sub> Perovskite Solar Cells. *Appl. Phys. Lett.* **2015**, *106*, 221104.

(57) Baloch, A. A. B.; Hossain, M. I.; Tabet, N.; Alharbi, F. H. Practical Efficiency Limit of Methylammonium Lead Iodide Perovskite (CH<sub>3</sub>NH<sub>3</sub>PbI<sub>3</sub>) Solar Cells. *J. Phys. Chem. Lett.* **2018**, *9*, 426–434.

(58) Pazos-Outón, L. M.; Xiao, T. P.; Yablonovitch, E. Fundamental Efficiency Limit of Lead Iodide Perovskite Solar Cells. *J. Phys. Chem. Lett.* **2018**, *9*, 1703–1711.

(59) Agresti, A.; Pescetelli, S.; Palma, A. L.; Del Rio Castillo, A. E.; Konios, D.; Kakavelakis, G.; Razza, S.; Cinà, L.; Kymakis, E.; Bonaccorso, F.; Di Carlo, A. Graphene Interface Engineering for

Perovskite Solar Modules: 12.6% Power Conversion Efficiency over 50 cm<sup>2</sup> Active Area. *ACS Energy Lett.* **2017**, *2*, 279–287.

(60) Agresti, A.; Pescetelli, S.; Taheri, B.; Del Rio Castillo, A. E.; Cina, L.; Bonaccorso, F.; Di Carlo, A. Graphene–Perovskite Solar Cells Exceed 18% Efficiency: A Stability Study. *ChemSusChem* **2016**, *9*, 2609–2619.

(61) Kakavelakis, G.; Maksudov, T.; Konios, D.; Kioseoglou, G.; Stratakis, E.; Kymakis, E. Efficient and Highly Air Stable Planar Inverted Perovskite Solar Cells with Reduced Graphene Oxide Doped PCBM Electron Transporting Layer. *Adv. Energy Mater.* **2017**, *7*, 1602120.

(62) Agresti, A.; Pescetelli, S.; Cina, L.; Dimitrios, K.; Kakavelakis, G.; Kymakis, E.; Di Carlo, A. Efficiency and Stability Enhancement in Perovskite Solar Cells by Inserting Lithium-Neutralized Graphene Oxide as Electron Transporting Layer. *Adv. Funct. Mater.* **2016**, *26*, 2686–2694.

(63) Cho, K. T.; Grancini, G.; Lee, Y.; Konios, D.; Paek, S.; Kymakis, E.; Nazeeruddin, M. K. T. Beneficial Role of Reduced Graphene Oxide for Electron Extraction in Highly Efficient Perovskite Solar Cells. *ChemSusChem* **2016**, *9*, 3040–3044.

(64) Capasso, A.; Matteocci, F.; Najafi, L.; Prato, M.; Buha, J.; Cinà, L.; Pellegrini, V.; Di Carlo, A.; Bonaccorso, F. Few-Layer MoS<sub>2</sub> Flakes as Active Buffer Layer for Stable Perovskite Solar Cells. *Adv. Energy Mater.* **2016**, *6*, 1600920.

(65) Shan, C.; Gaoquan, S. Two-Dimensional Materials for Halide Perovskite-Based Optoelectronic Devices. *Adv. Mater.* **2017**, *29*, 1605448.

(66) Van Le, Q.; Choi, J.-Y.; Kim, S. Y. Recent Advances in the Application of Two-Dimensional Materials as Charge Transport Layers in Organic and Perovskite Solar Cells. *FlatChem* **2017**, *2*, 54–66.

(67) Chen, W.; Li, K.; Wang, Y.; Feng, X.; Liao, Z.; Su, Q.; Lin, X.; He, Z. Black Phosphorus Quantum Dots for Hole Extraction of Typical Planar Hybrid Perovskite Solar Cells. *J. Phys. Chem. Lett.* **2017**, *8*, 591–598.

(68) Muduli, S. K.; Varrla, E.; Kulkarni, S. A.; Han, G.; Thirumal, K.; Lev, O.; Mhaisalkar, S.; Mathews, N. 2D Black Phosphorous Nanosheets as a Hole Transporting Material in Perovskite Solar Cells. *J. Power Sources* **2017**, *371*, 156–161.

(69) Biccari, F.; Gabelloni, F.; Burzi, E.; Gurioli, M.; Pescetelli, S.; Agresti, A.; Del Rio Castillo, A. E.; Ansaldo, A.; Kymakis, E.; Bonaccorso, F.; Di Carlo, A. Graphene-Based Electron Transport Layers in Perovskite Solar Cells: A Step-Up for an Efficient Carrier Collection. *Adv. Energy Mater.* **2017**, *7*, 1701349.

(70) Ruina, D.; Yangyang, W.; Jie, W.; Xianyu, D. Metal–Organic-Compound-Modified MoS<sub>2</sub> with Enhanced Solubility for High-Performance Perovskite Solar Cells. *ChemSusChem* **2017**, *10*, 2869–2874.

(71) Kakvelakis, G.; Paradisanos, I.; Paci, B.; Generosi, A.; Papachatzakis, M.; Maksukov, T.; Najafi, L.; Del Rio Castillo, A. E.; Kioseoglou, G.; Stratakis, E.; Bonaccorso, F.; Kymakis, E. Extending the Continuous Operating Lifetime of Perovskite Solar Cells with a Molybdenum Disulfide Hole Extraction Interlayer. *Adv. Energy Mater.* **2018**, *8*, 1702287.

(72) Dasgupta, U.; Chatterjee, S.; Pal, A. J. Thin-Film Formation of 2D MoS<sub>2</sub> and Its Application as a Hole-Transport Layer in Planar Perovskite Solar Cells. *Sol. Energy Mater. Sol. Cells* **2017**, *172*, 353–360.

(73) Kuila, T.; Bose, S.; Mishra, A. K.; Khanra, P.; Kim, N. H.; Lee, J. H. Chemical Functionalization of Graphene and Its Applications. *Prog. Mater. Sci.* **2012**, *57*, 1061–1105.

(74) Ferrari, A. C.; Bonaccorso, F.; Fal'ko, V.; Novoselov, K. S.; Roche, S.; Bøggild, P.; Borini, S.; Koppens, F. H. L.; Palermo, V.; Pugno, N.; Garrido, J. A.; Sordan, R.; Bianco, A.; Ballerini, L.; Prato, M.; Lidorikis, E.; Kivioja, J.; Marinelli, C.; Ryhänen, T.; Morpurgo, A.; et al. Science and Technology Roadmap for Graphene, Related Two-Dimensional Crystals, and Hybrid Systems. *Nanoscale* **2015**, *7*, 4598–4810.

(75) Xiaodong, Z.; Yiyong, M.; Dongqing, W.; Fan, Z.; Xinliang, F. Two-Dimensional Soft Nanomaterials: A Fascinating World of Materials. *Adv. Mater.* **2015**, *27*, 403–427.

(76) Terrones, M.; Botello-Méndez, A. R.; Campos-Delgado, J.; López-Urías, F.; Vega-Cantú, Y. I.; Rodríguez-Macías, F. J.; Elías, A. L.; Muñoz-Sandoval, E.; Cano-Márquez, A. G.; Charlier, J.-C.; Terrones, H. Graphene and Graphite Nanoribbons: Morphology, Properties, Synthesis, Defects and Applications. *Nano Today* **2010**, *5*, 351–372.

(77) Jia, X.; Campos-Delgado, J.; Terrones, M.; Meunier, V.; Dresselhaus, M. S. Graphene Edges: A Review of Their Fabrication and Characterization. *Nanoscale* **2011**, *3*, 86–95.

(78) Samori, P.; Palermo, V.; Feng, X. Chemical Approaches to 2D Materials. *Adv. Mater.* **2016**, *28*, 6027–6029.

(79) Georgakilas, V.; Otyepka, M.; Bourlino, A. B.; Chandra, V.; Kim, N.; Kemp, K. C.; Hobza, P.; Zboril, R.; Kim, K. S. Functionalization of Graphene: Covalent and Non-Covalent Approaches, Derivatives and Applications. *Chem. Rev.* **2012**, *112*, 6156–6214.

(80) Chhowalla, M.; Shin, H. S.; Eda, G.; Li, L.-J.; Loh, K. P.; Zhang, H. The Chemistry of Two-Dimensional Layered Transition Metal Dichalcogenide Nanosheets. *Nat. Chem.* **2013**, *5*, 263.

(81) Nicolosi, V.; Chhowalla, M.; Kanatzidis, M. G.; Strano, M. S.; Coleman, J. N. Liquid Exfoliation of Layered Materials. *Science* **2013**, *340*, 1226419.

(82) Ciesielski, A.; Samori, P. Graphene via Sonication Assisted Liquid-Phase Exfoliation. *Chem. Soc. Rev.* **2014**, *43*, 381–398.

(83) Parvez, K.; Yang, S.; Feng, X.; Müllen, K. Exfoliation of Graphene via Wet Chemical Routes. *Synth. Met.* **2015**, *210*, 123–132.

(84) Bonaccorso, F.; Lombardo, A.; Hasan, T.; Sun, Z.; Colombo, L.; Ferrari, A. C. Production and Processing of Graphene and 2d Crystals. *Mater. Today* **2012**, *15*, 564–589.

(85) Del Rio Castillo, A. E.; Pellegrini, V.; Ansaldo, A.; Ricciardella, F.; Sun, H.; Marasco, L.; Buha, J.; Dang, Z.; Gagliani, L.; Lago, E.; Bonaccorso, F. High-Yield Production of 2D Crystals by Wet-Jet Milling. *Mater. Horiz.* **2018**, *5*, 890–904.

(86) Bonaccorso, F.; Bartolotta, A.; Coleman, J. N.; Backes, C. 2D-Crystal-Based Functional Inks. *Adv. Mater.* **2016**, *28*, 6136–6166.

(87) Tung, V. C.; Allen, M. J.; Yang, Y.; Kaner, R. B. High-Throughput Solution Processing of Large-Scale Graphene. *Nat. Nanotechnol.* **2009**, *4*, 25.

(88) Li, D.; Müller, M. B.; Gilje, S.; Kaner, R. B.; Wallace, G. G. Processable Aqueous Dispersions of Graphene Nanosheets. *Nat. Nanotechnol.* **2008**, *3*, 101.

(89) Torrisi, F.; Hasan, T.; Wu, W.; Sun, Z.; Lombardo, A.; Kulmala, T. S.; Hsieh, G.-W.; Jung, S.; Bonaccorso, F.; Paul, P. J.; Chu, D. Inkjet-Printed Graphene Electronics. *ACS Nano* **2012**, *6*, 2992–3006.

(90) Secor, E. B.; Lim, S.; Zhang, H.; Frisbie, C. D.; Francis, L. F.; Hersam, M. C. Gravure Printing of Graphene for Large-Area Flexible Electronics. *Adv. Mater.* **2014**, *26*, 4533–4538.

(91) You, J.; Hong, Z.; Yang, Y.; Chen, Q.; Cai, M.; Song, T.-B.; Chen, C.-C.; Lu, S.; Liu, Y.; Zhou, H.; Yang, Y. Low-Temperature Solution-Processed Perovskite Solar Cells with High Efficiency and Flexibility. *ACS Nano* **2014**, *8*, 1674–1680.

(92) Tan, H.; Jain, A.; Voznyy, O.; Lan, X.; García de Arquer, F. P.; Fan, J. Z.; Quintero-Bermudez, R.; Yuan, M.; Zhang, B.; Zhao, Y.; Fan, F. Efficient and Stable Solution-Processed Planar Perovskite Solar Cells via Contact Passivation. *Science* **2017**, *355*, 722–726.

(93) Chueh, C.-C.; Li, C.-Z.; Jen, A. K.-Y. Recent Progress and Perspective in Solution-Processed Interfacial Materials for Efficient and Stable Polymer and Organometal Perovskite Solar Cells. *Energy Environ. Sci.* **2015**, *8*, 1160–1189.

(94) Singh, E.; Kim, K. S.; Yeom, G. Y.; Nalwa, H. S. Atomically Thin-Layered Molybdenum Disulfide (MoS<sub>2</sub>) for Bulk-Heterojunction Solar Cells. *ACS Appl. Mater. Interfaces* **2017**, *9*, 3223–3245.

(95) Bellani, S.; Najafi, L.; Capasso, A.; Del Rio Castillo, A. E.; Antognazza, M. R.; Bonaccorso, F. Few-Layer MoS<sub>2</sub> Flakes as a Hole-Selective Layer for Solution-Processed Hybrid Organic Hydrogen-Evolving Photocathodes. *J. Mater. Chem. A* **2017**, *5*, 4384–4396.

- (96) Capasso, A.; Del Rio Castillo, A. E.; Najafi, L.; Pellegrini, V.; Bonaccorso, F.; Matteocci, F.; Cinà, L.; Di Carlo, A. Spray Deposition of Exfoliated MoS<sub>2</sub> Flakes as Hole Transport Layer in Perovskite-Based Photovoltaics. In *2015 IEEE 15th International Conference on Nanotechnology (IEEE-NANO)*; 2015; pp 1138–1141.
- (97) Kohnepoushi, S.; Nazari, P.; Nejang, B. A.; Eskandari, M. MoS<sub>2</sub>: A Two-Dimensional Hole-Transporting Material for High-Efficiency, Low-Cost Perovskite Solar Cells. *Nanotechnology* **2018**, *29*, 205201.
- (98) Xing, G.; Wei, C.; Hai, L.; Zhongwei, W.; Zhiyuan, Z.; Shuitong, L.; Hua, Z.; Baoquan, S. A Solution-Processed Hole Extraction Layer Made from Ultrathin MoS<sub>2</sub> Nanosheets for Efficient Organic Solar Cells. *Adv. Energy Mater.* **2013**, *3*, 1262–1268.
- (99) Xing, W.; Chen, Y.; Wang, X.; Lv, L.; Ouyang, X.; Ge, Z.; Huang, H. MoS<sub>2</sub> Quantum Dots with a Tunable Work Function for High-Performance Organic Solar Cells. *ACS Appl. Mater. Interfaces* **2016**, *8*, 26916–26923.
- (100) Wu, Z.; Bai, S.; Xiang, J.; Yuan, Z.; Yang, Y.; Cui, W.; Gao, X.; Liu, Z.; Jin, Y.; Sun, B. Efficient Planar Heterojunction Perovskite Solar Cells Employing Graphene Oxide as Hole Conductor. *Nanoscale* **2014**, *6*, 10505–10510.
- (101) Yan, K.; Wei, Z.; Li, J.; Chen, H.; Yi, Y.; Zheng, X.; Long, X.; Wang, Z.; Wang, J.; Xu, J.; Yang, S. High-Performance Graphene-Based Hole Conductor-Free Perovskite Solar Cells: Schottky Junction Enhanced Hole Extraction and Electron Blocking. *Small* **2015**, *11*, 2269–2274.
- (102) Palma, A. L.; Cinà, L.; Pescetelli, S.; Agresti, A.; Raggio, M.; Paolesse, R.; Bonaccorso, F.; Di Carlo, A. Reduced Graphene Oxide as Efficient and Stable Hole Transporting Material in Mesoscopic Perovskite Solar Cells. *Nano Energy* **2016**, *22*, 349–360.
- (103) Yeo, J.-S.; Kang, R.; Lee, S.; Jeon, Y.-J.; Myoung, N.; Lee, C.-L.; Kim, D.-Y.; Yun, J.-M.; Seo, Y.-H.; Kim, S.-S.; Na, S. I. Highly Efficient and Stable Planar Perovskite Solar Cells with Reduced Graphene Oxide Nanosheets as Electrode Interlayer. *Nano Energy* **2015**, *12*, 96–104.
- (104) Arora, N.; Dar, M. I.; Hinderhofer, A.; Pellet, N.; Schreiber, F.; Zakeeruddin, S. M.; Grätzel, M. Perovskite Solar Cells with CuSCN Hole Extraction Layers Yield Stabilized Efficiencies Greater than 20%. *Science* **2017**, *358*, 768–771.
- (105) Nouri, E.; Wang, Y.-L.; Chen, Q.; Xu, J.-J.; Paterakis, G.; Dracopoulos, V.; Xu, Z.-X.; Tasis, D.; Mohammadi, M. R.; Lianos, P. Introduction of Graphene Oxide as Buffer Layer in Perovskite Solar Cells and the Promotion of Soluble N-Butyl-Substituted Copper Phthalocyanine as Efficient Hole Transporting Material. *Electrochim. Acta* **2017**, *233*, 36–43.
- (106) Lee, S. Y.; Kim, U. J.; Chung, J.; Nam, H.; Jeong, H. Y.; Han, G. H.; Kim, H.; Oh, H. M.; Lee, H.; Kim, H.; Roh, Y. G. Large Work Function Modulation of Monolayer MoS<sub>2</sub> by Ambient Gases. *ACS Nano* **2016**, *10*, 6100–6107.
- (107) Zhou, P.; Song, X.; Yan, X.; Liu, C.; Chen, L.; Sun, Q.; Zhang, D. W. Controlling the Work Function of Molybdenum Disulfide by *in Situ* Metal Deposition. *Nanotechnology* **2016**, *27*, 344002.
- (108) Baik, S. S.; Im, S.; Choi, H. J. Work Function Tuning in Two-Dimensional MoS<sub>2</sub> Field-Effect-Transistors with Graphene and Titanium Source-Drain Contacts. *Sci. Rep.* **2017**, *7*, 45546.
- (109) Kim, J. H.; Lee, J.; Kim, J. H.; Hwang, C. C.; Lee, C.; Park, J. Y. Work Function Variation of MoS<sub>2</sub> Atomic Layers Grown with Chemical Vapor Deposition: The Effects of Thickness and the Adsorption of Water/oxygen Molecules. *Appl. Phys. Lett.* **2015**, *106*, 251606.
- (110) Shi, Y.; Kim, K. K.; Reina, A.; Hofmann, M.; Li, L.-J.; Kong, J. Work Function Engineering of Graphene Electrode *via* Chemical Doping. *ACS Nano* **2010**, *4*, 2689–2694.
- (111) Chang, K. K.; Soon, C. K.; Young, K. S. Increased Work Function in Few-Layer Graphene Sheets *via* Metal Chloride Doping. *Adv. Funct. Mater.* **2012**, *22*, 4724–4731.
- (112) Garg, R.; Dutta, K. N.; Choudhury, R. N. Work Function Engineering of Graphene. *Nanomaterials* **2014**, *4*, 267.
- (113) Sygellou, L.; Paterakis, G.; Galiotis, C.; Tasis, D. Work Function Tuning of Reduced Graphene Oxide Thin Films. *J. Phys. Chem. C* **2016**, *120*, 281–290.
- (114) Harwell, J. R.; Baikie, T. K.; Baikie, I. D.; Payne, J. L.; Ni, C.; Irvine, J. T. S.; Turnbull, G. A.; Samuel, I. D. W. Probing the Energy Levels of Perovskite Solar Cells *via* Kelvin Probe and UV Ambient Pressure Photoemission Spectroscopy. *Phys. Chem. Chem. Phys.* **2016**, *18*, 19738–19745.
- (115) Nguyen, W. H.; Bailie, C. D.; Unger, E. L.; McGehee, M. D. Enhancing the Hole-Conductivity of Spiro-OMeTAD without Oxygen or Lithium Salts by Using Spiro(TFSI)<sub>2</sub> in Perovskite and Dye-Sensitized Solar Cells. *J. Am. Chem. Soc.* **2014**, *136*, 10996–11001.
- (116) Saygili, Y.; Turren-Cruz, S. H.; Olthof, S.; Saes, B. W. H.; Pehlivan, I. B.; Saliba, M.; Meerholz, K.; Edvinsson, T.; Zakeeruddin, S. M.; Grätzel, M.; Correa-Baena, J. P. Planar Perovskite Solar Cells with High Open-Circuit Voltage Containing a Supramolecular Iron Complex as Hole Transport Material Dopant. *ChemPhysChem* **2018**, *19*, 1363–1370.
- (117) Schölin, R.; Karlsson, M. H.; Eriksson, S. K.; Siegbahn, H.; Johansson, E. M. J.; Rensmo, H. Energy Level Shifts in Spiro-OMeTAD Molecular Thin Films When Adding Li-TFSI. *J. Phys. Chem. C* **2012**, *116*, 26300–26305.
- (118) Nardes, A. M.; Kemerink, M.; de Kok, M. M.; Vinken, E.; Maturova, K.; Janssen, R. A. J. Conductivity, Work Function, and Environmental Stability of PEDOT:PSS Thin Films Treated with Sorbitol. *Org. Electron.* **2008**, *9*, 727–734.
- (119) Huang, J.; Miller, P. F.; Wilson, J. S.; de Mello, A. J.; de Mello, J. C.; Bradley, D. D. C. Investigation of the Effects of Doping and Post-Deposition Treatments on the Conductivity, Morphology, and Work Function of Poly(3,4-ethylenedioxythiophene)/Poly(styrene Sulfonate) Films. *Adv. Funct. Mater.* **2005**, *15*, 290–296.
- (120) Hwang, J.; Amy, F.; Kahn, A. Spectroscopic Study on Sputtered PEDOT:PSS: Role of Surface PSS Layer. *Org. Electron.* **2006**, *7*, 387–396.
- (121) Brown, T. M.; Kim, J. S.; Friend, R. H.; Caciagli, F.; Daik, R.; Feast, W. J. Built-in Field Electroabsorption Spectroscopy of Polymer Light-Emitting Diodes Incorporating a Doped poly(3,4-Ethylene Dioxothiophene) Hole Injection Layer. *Appl. Phys. Lett.* **1999**, *75*, 1679–1681.
- (122) Jun, L.; Yuhua, X.; Yunxiang, G.; Dingshan, Y.; Michael, D.; Liming, D. Hole and Electron Extraction Layers Based on Graphene Oxide Derivatives for High-Performance Bulk Heterojunction Solar Cells. *Adv. Mater.* **2012**, *24*, 2228–2233.
- (123) Lin, Y.; Li, X.; Xie, D.; Feng, T.; Chen, Y.; Song, R.; Tian, H.; Ren, T.; Zhong, M.; Wang, K.; Zhu, H. Graphene/semiconductor Heterojunction Solar Cells with Modulated Antireflection and Graphene Work Function. *Energy Environ. Sci.* **2013**, *6*, 108–115.
- (124) Huang, H.; Li, Z.; She, J.; Wang, W. Oxygen Density Dependent Band Gap of Reduced Graphene Oxide. *J. Appl. Phys.* **2012**, *111*, 54317.
- (125) Shen, Y.; Yang, S.; Zhou, P.; Sun, Q.; Wang, P.; Wan, L.; Li, J.; Chen, L.; Wang, X.; Ding, S.; Zhang, D. W. Evolution of the Band-Gap and Optical Properties of Graphene Oxide with Controllable Reduction Level. *Carbon* **2013**, *62*, 157–164.
- (126) Ellis, J. K.; Lucero, M. J.; Scuseria, G. E. The Indirect to Direct Band Gap Transition in Multilayered MoS<sub>2</sub> as Predicted by Screened Hybrid Density Functional Theory. *Appl. Phys. Lett.* **2011**, *99*, 261908.
- (127) Yun, W. S.; Han, S. W.; Hong, S. C.; Kim, I. G.; Lee, J. D. Thickness and Strain Effects on Electronic Structures of Transition Metal Dichalcogenides: 2H-MX<sub>2</sub> Semiconductors (M = Mo, W; X = S, Se, Te). *Phys. Rev. B: Condens. Matter Mater. Phys.* **2012**, *85*, 033305.
- (128) Mak, K. F.; Lee, C.; Hone, J.; Shan, J.; Heinz, T. F. Atomically Thin MoS<sub>2</sub>: A New Direct-Gap Semiconductor. *Phys. Rev. Lett.* **2010**, *105*, 136805.
- (129) Han, S. W.; Kwon, H.; Kim, S. K.; Ryu, S.; Yun, W. S.; Kim, D. H.; Hwang, J. H.; Kang, J.-S.; Baik, J.; Shin, H. J.; Hong, S. C. Band-

Gap Transition Induced by Interlayer van Der Waals Interaction in MoS<sub>2</sub>. *Phys. Rev. B: Condens. Matter Mater. Phys.* **2011**, *84*, 045409.

(130) Wang, Q. H.; Kalantar-Zadeh, K.; Kis, A.; Coleman, J. N.; Strano, M. S. Electronics and Optoelectronics of Two-Dimensional Transition Metal Dichalcogenides. *Nat. Nanotechnol.* **2012**, *7*, 699.

(131) Kang, J.; Tongay, S.; Zhou, J.; Li, J.; Wu, J. Band Offsets and Heterostructures of Two-Dimensional Semiconductors. *Appl. Phys. Lett.* **2013**, *102*, 12111.

(132) Wu, M.; Yao, X.; Hao, Y.; Dong, H.; Cheng, Y.; Liu, H.; Lu, F.; Wang, W.; Cho, K.; Wang, W.-H. Electronic Structures, Magnetic Properties and Band Alignments of 3d Transition Metal Atoms Doped Monolayer MoS<sub>2</sub>. *Phys. Lett. A* **2018**, *382*, 111–115.

(133) Rasmussen, F. A.; Thygesen, K. S. Computational 2D Materials Database: Electronic Structure of Transition-Metal Dichalcogenides and Oxides. *J. Phys. Chem. C* **2015**, *119*, 13169–13183.

(134) Qiu, J.; Qiu, Y.; Yan, K.; Zhong, M.; Mu, C.; Yan, H.; Yang, S. All-Solid-State Hybrid Solar Cells Based on a New Organometal Halide Perovskite Sensitizer and One-Dimensional TiO<sub>2</sub> Nanowire Arrays. *Nanoscale* **2013**, *5*, 3245–3248.

(135) Yang, G.; Tao, H.; Qin, P.; Ke, W.; Fang, G. Recent Progress in Electron Transport Layers for Efficient Perovskite Solar Cells. *J. Mater. Chem. A* **2016**, *4*, 3970–3990.

(136) Kim, H.-S.; Lee, C.-R.; Im, J.-H.; Lee, K.-B.; Moehl, T.; Marchioro, A.; Moon, S.-J.; Humphry-Baker, R.; Yum, J.-H.; Moser, J. E.; Grätzel, M. Lead Iodide Perovskite Sensitized All-Solid-State Submicron Thin Film Mesoscopic Solar Cell with Efficiency Exceeding 9%. *Sci. Rep.* **2012**, *2*, 591.

(137) Hao, F.; Stoumpos, C. C.; Chang, R. P. H.; Kanatzidis, M. G. Anomalous Band Gap Behavior in Mixed Sn and Pb Perovskites Enables Broadening of Absorption Spectrum in Solar Cells. *J. Am. Chem. Soc.* **2014**, *136*, 8094–8099.

(138) Olthof, S. Research Update: The Electronic Structure of Hybrid Perovskite Layers and Their Energetic Alignment in Devices. *APL Mater.* **2016**, *4*, 91502.

(139) Schulz, P.; Whittaker-Brooks, L.; MacLeod, B.; Olson, D.; Yueh-Lin, L.; Antoine, K. Electronic Level Alignment in Inverted Organometal Perovskite Solar Cells. *Adv. Mater. Interfaces* **2015**, *2*, 1400532.

(140) Ratcliff, E. L.; Garcia, A.; Paniagua, S. A.; Cowan, S. R.; Giordano, A. J.; Ginley, D. S.; Marder, S. R.; Berry, J. J.; Olson, D. C. Investigating the Influence of Interfacial Contact Properties on Open Circuit Voltages in Organic Photovoltaic Performance: Work Function Versus Selectivity. *Adv. Energy Mater.* **2013**, *3*, 647–656.

(141) Steim, R.; Choulis, S. A.; Schilinsky, P.; Brabec, C. J. Interface Modification for Highly Efficient Organic Photovoltaics. *Appl. Phys. Lett.* **2008**, *92*, 93303.

(142) Zhong, H.; Quhe, R.; Wang, Y.; Ni, Z.; Ye, M.; Song, Z.; Pan, Y.; Yang, J.; Yang, L.; Lei, M.; Shi, J. Interfacial Properties of Monolayer and Bilayer MoS<sub>2</sub> Contacts with Metals: Beyond the Energy Band Calculations. *Sci. Rep.* **2016**, *6*, 21786.

(143) Yun, J.-M.; Noh, Y.-J.; Yeo, J.-S.; Go, Y.-J.; Na, S.-I.; Jeong, H.-G.; Kim, J.; Lee, S.; Kim, S.-S.; Koo, H. Y.; Kim, T. W. Efficient Work-Function Engineering of Solution-Processed MoS<sub>2</sub> Thin-Films for Novel Hole and Electron Transport Layers Leading to High-Performance Polymer Solar Cells. *J. Mater. Chem. C* **2013**, *1*, 3777–3783.

(144) Najafi, L.; Bellani, S.; Martín-García, B.; Oropesa-Nuñez, R.; Del Rio Castillo, A. E.; Prato, M.; Moreels, I.; Bonaccorso, F. Solution-Processed Hybrid Graphene Flake/2H-MoS<sub>2</sub> Quantum Dot Heterostructures for Efficient Electrochemical Hydrogen Evolution. *Chem. Mater.* **2017**, *29*, 5782–5786.

(145) Sun, Y.; Takacs, C. J.; Cowan, S. R.; Seo, J. H.; Gong, X.; Roy, A.; Heeger, A. J. Efficient, Air-Stable Bulk Heterojunction Polymer Solar Cells Using MoO<sub>x</sub> as the Anode Interfacial Layer. *Adv. Mater.* **2011**, *23*, 2226–2230.

(146) Fumagalli, F.; Bellani, S.; Schreier, M.; Leonardi, S.; Rojas, H. C.; Ghadirzadeh, A.; Tullii, G.; Savoini, A.; Marra, G.; Meda, L.; Grätzel, M.; Lanzani, G.; Mayer, M. T.; Antognazza, M. R.; Di Fonzo,

F. Hybrid Organic–inorganic H<sub>2</sub>-Evolving Photocathodes: Understanding the Route towards High Performance Organic Photoelectrochemical Water Splitting. *J. Mater. Chem. A* **2016**, *4*, 2178–2187.

(147) Chen, L.-M.; Xu, Z.; Hong, Z.; Yang, Y. Interface Investigation and Engineering – Achieving High Performance Polymer Photovoltaic Devices. *J. Mater. Chem.* **2010**, *20*, 2575.

(148) Lu, C.-P.; Li, G.; Mao, J.; Wang, L.-M.; Andrei, E. Y. Bandgap, Mid-Gap States, and Gating Effects in MoS<sub>2</sub>. *Nano Lett.* **2014**, *14*, 4628–4633.

(149) Fivaz, R.; Mooser, E. Mobility of Charge Carriers in Semiconducting Layer Structures. *Phys. Rev.* **1967**, *163*, 743–755.

(150) El-Mahalawy, S.; Evans, B. Temperature Dependence of the Electrical Conductivity and Hall Coefficient in 2H-MoS<sub>2</sub>, MoSe<sub>2</sub>, WSe<sub>2</sub>, and MoTe<sub>2</sub>. *Phys. Status Solidi B* **2018**, *79*, 713–722.

(151) Dolui, K.; Rungger, I.; Sanvito, S. Origin of the N-Type and P-Type Conductivity of MoS<sub>2</sub> Monolayers on a SiO<sub>2</sub> Substrate. *Phys. Rev. B: Condens. Matter Mater. Phys.* **2013**, *87*, 165402.

(152) Yuan, S.; Roldán, R.; Katsnelson, M. I.; Guinea, F. Effect of Point Defects on the Optical and Transport Properties of MoS<sub>2</sub> and WS<sub>2</sub>. *Phys. Rev. B: Condens. Matter Mater. Phys.* **2014**, *90*, 041402.

(153) Vancsó, P.; Magda, G. Z.; Pető, J.; Noh, J.-Y.; Kim, Y.-S.; Hwang, C.; Biró, L. P.; Tapasztó, L. The Intrinsic Defect Structure of Exfoliated MoS<sub>2</sub> Single Layers Revealed by Scanning Tunneling Microscopy. *Sci. Rep.* **2016**, *6*, 29726.

(154) Cho, K.; Min, M.; Kim, T.-Y.; Jeong, H.; Pak, J.; Kim, J.-K.; Jang, J.; Yun, S. J.; Lee, Y. H.; Hong, W.-K.; Lee, T. Electrical and Optical Characterization of MoS<sub>2</sub> with Sulfur Vacancy Passivation by Treatment with Alkanethiol Molecules. *ACS Nano* **2015**, *9*, 8044–8053.

(155) Liu, D.; Guo, Y.; Fang, L.; Robertson, J. Sulfur Vacancies in Monolayer MoS<sub>2</sub> and Its Electrical Contacts. *Appl. Phys. Lett.* **2013**, *103*, 183113.

(156) Le, D.; Rawal, T. B.; Rahman, T. S. Single-Layer MoS<sub>2</sub> with Sulfur Vacancies: Structure and Catalytic Application. *J. Phys. Chem. C* **2014**, *118*, 5346–5351.

(157) Qiu, H.; Xu, T.; Wang, Z.; Ren, W.; Nan, H.; Ni, Z.; Chen, Q.; Yuan, S.; Miao, F.; Song, F.; Long, G. Hopping Transport through Defect-Induced Localized States in Molybdenum Disulfide. *Nat. Commun.* **2013**, *4*, 2642.

(158) Fabbri, F.; Rotunno, E.; Cinquanta, E.; Campi, D.; Bonnini, E.; Kaplan, D.; Lazzarini, L.; Bernasconi, M.; Ferrari, C.; Longo, M.; Nicotra, G. Novel near-Infrared Emission from Crystal Defects in MoS<sub>2</sub> Multilayer Flakes. *Nat. Commun.* **2016**, *7*, 13044.

(159) Yin, Z.; Li, H.; Li, H.; Jiang, L.; Shi, Y.; Sun, Y.; Lu, G.; Zhang, Q.; Chen, X.; Zhang, H. Single-Layer MoS<sub>2</sub> Phototransistors. *ACS Nano* **2012**, *6*, 74–80.

(160) Yung-Chang, L.; O, D. D.; Hannu-Pekka, K.; Yoshiko, N.; V, K. A.; Ying-Sheng, H.; Kazu, S. Properties of Individual Dopant Atoms in Single-Layer MoS<sub>2</sub>: Atomic Structure, Migration, and Enhanced Reactivity. *Adv. Mater.* **2014**, *26*, 2857–2861.

(161) Baugher, B. W. H.; Churchill, H. O. H.; Yang, Y.; Jarillo-Herrero, P. Intrinsic Electronic Transport Properties of High-Quality Monolayer and Bilayer MoS<sub>2</sub>. *Nano Lett.* **2013**, *13*, 4212–4216.

(162) McDonnell, S.; Addou, R.; Buie, C.; Wallace, R. M.; Hinkle, C. L. Defect-Dominated Doping and Contact Resistance in MoS<sub>2</sub>. *ACS Nano* **2014**, *8*, 2880–2888.

(163) Zhou, W.; Zou, X.; Najmaei, S.; Liu, Z.; Shi, Y.; Kong, J.; Lou, J.; Ajayan, P. M.; Yakobson, B. I.; Idrobo, J.-C. Intrinsic Structural Defects in Monolayer Molybdenum Disulfide. *Nano Lett.* **2013**, *13*, 2615–2622.

(164) Santosh, K. C.; Longo, R. C.; Addou, R.; Wallace, R. M.; Cho, K. Impact of Intrinsic Atomic Defects on the Electronic Structure of MoS<sub>2</sub> Monolayers. *Nanotechnology* **2014**, *25*, 375703.

(165) Zhao, Y.; Nardes, A. M.; Zhu, K. Solid-State Mesostuctured Perovskite CH<sub>3</sub>NH<sub>3</sub>PbI<sub>3</sub> Solar Cells: Charge Transport, Recombination, and Diffusion Length. *J. Phys. Chem. Lett.* **2014**, *5*, 490–494.

(166) Martín-García, B.; Polovitsyn, A.; Prato, M.; Moreels, I. Efficient Charge Transfer in Solution-Processed PbS Quantum Dot–

reduced Graphene Oxide Hybrid Materials. *J. Mater. Chem. C* **2015**, *3*, 7088–7095.

(167) Hou, S.; Su, S.; Kasner, M. L.; Shah, P.; Patel, K.; Madarang, C. J. Formation of Highly Stable Dispersions of Silane-Functionalized Reduced Graphene Oxide. *Chem. Phys. Lett.* **2010**, *501*, 68–74.

(168) Yao, H.; Jin, L.; Sue, H.-J.; Sumi, Y.; Nishimura, R. Facile Decoration of Au Nanoparticles on Reduced Graphene Oxide Surfaces via a One-Step Chemical Functionalization Approach. *J. Mater. Chem. A* **2013**, *1*, 10783.

(169) Chen, X.; Berner, N. C.; Backes, C.; Duesberg, G. S.; McDonald, A. R. Functionalization of Two-Dimensional MoS<sub>2</sub>: On the Reaction Between MoS<sub>2</sub> and Organic Thiols. *Angew. Chem., Int. Ed.* **2016**, *55*, 5803–5808.

(170) Förster, A.; Gemming, S.; Seifert, G.; Tománek, D. Chemical and Electronic Repair Mechanism of Defects in MoS<sub>2</sub> Monolayers. *ACS Nano* **2017**, *11*, 9989–9996.

(171) Ding, Q.; Czech, K. J.; Zhao, Y.; Zhai, J.; Hamers, R. J.; Wright, J. C.; Jin, S. Basal-Plane Ligand Functionalization on Semiconducting 2H-MoS<sub>2</sub> Monolayers. *ACS Appl. Mater. Interfaces* **2017**, *9*, 12734–12742.

(172) Green, A. A.; Hersam, M. C. Solution Phase Production of Graphene with Controlled Thickness via Density Differentiation. *Nano Lett.* **2009**, *9*, 4031–4036.

(173) Sun, X.; Luo, D.; Liu, J.; Evans, D. G. Monodisperse Chemically Modified Graphene Obtained by Density Gradient Ultracentrifugal Rate Separation. *ACS Nano* **2010**, *4*, 3381–3389.

(174) Björkman, T.; Gulans, A.; Krashennikov, A. V.; Nieminen, R. M. Van Der Waals Bonding in Layered Compounds from Advanced Density-Functional First-Principles Calculations. *Phys. Rev. Lett.* **2012**, *108*, 235502.

(175) Toulhoat, P. R.; Raybaud, P.; Kresse, G.; Hafner, J. *Ab Initio* Density Functional Studies of Transition-Metal Sulphides: I. Crystal Structure and Cohesive Properties. *J. Phys.: Condens. Matter* **1997**, *9*, 11085.

(176) Bučko, T.; Hafner, J.; Lebègue, S.; Ángyán, J. G. Improved Description of the Structure of Molecular and Layered Crystals: *Ab Initio* DFT Calculations with van Der Waals Corrections. *J. Phys. Chem. A* **2010**, *114*, 11814–11824.

(177) Jawaid, A.; Nepal, D.; Park, K.; Jespersen, M.; Qualley, A.; Mirau, P.; Drummy, L. F.; Vaia, R. A. Mechanism for Liquid Phase Exfoliation of MoS<sub>2</sub>. *Chem. Mater.* **2016**, *28*, 337–348.

(178) Shen, J.; He, Y.; Wu, J.; Gao, C.; Keyshar, K.; Zhang, X.; Yang, Y.; Ye, M.; Vajtai, R.; Lou, J.; Ajayan, P. M. Liquid Phase Exfoliation of Two-Dimensional Materials by Directly Probing and Matching Surface Tension Components. *Nano Lett.* **2015**, *15*, 5449–5454.

(179) Bonaccorso, F.; Zerbetto, M.; Ferrari, A. C.; Amendola, V. Sorting Nanoparticles by Centrifugal Fields in Clean Media. *J. Phys. Chem. C* **2013**, *117*, 13217–13229.

(180) Gao, X.; Jang, J.; Nagase, S. Hydrazine and Thermal Reduction of Graphene Oxide: Reaction Mechanisms, Product Structures, and Reaction Design. *J. Phys. Chem. C* **2010**, *114*, 832–842.

(181) Pei, S.; Cheng, H.-M. The Reduction of Graphene Oxide. *Carbon* **2012**, *50*, 3210–3228.

(182) Hummers, W. S.; Offeman, R. E. Preparation of Graphitic Oxide. *J. Am. Chem. Soc.* **1958**, *80*, 1339.

(183) Bellani, S.; Najafi, L.; Martín-García, B.; Ansaldo, A.; Del Rio Castillo, A. E.; Prato, M.; Moreels, I.; Bonaccorso, F. Graphene-Based Hole-Selective Layers for High-Efficiency, Solution-Processed, Large-Area, Flexible, Hydrogen-Evolving Organic Photocathodes. *J. Phys. Chem. C* **2017**, *121*, 21887–21903.

(184) Zhang, X.; Coleman, A. C.; Katsonis, N.; Browne, W. R.; van Wees, B. J.; Feringa, B. L. Dispersion of Graphene in Ethanol Using a Simple Solvent Exchange Method. *Chem. Commun.* **2010**, *46*, 7539–7541.

(185) Sun, H.; Del Rio Castillo, A. E.; Monaco, S.; Capasso, A.; Ansaldo, A.; Prato, M.; Dinh, D. A.; Pellegrini, V.; Scrosati, B.; Manna, L.; Bonaccorso, F. Binder-Free Graphene as an Advanced Anode for Lithium Batteries. *J. Mater. Chem. A* **2016**, *4*, 6886–6895.

(186) Gao, W. *The Chemistry of Graphene Oxide: Graphene Oxide: Reduction Recipes, Spectroscopy, and Applications*; Gao, W., Ed.; Springer International Publishing: Cham, 2015; pp 61–95.

(187) Pham, N. P.; Burghartz, J. N.; Sarro, P. M. Spray Coating of Photoresist for Pattern Transfer on High Topography Surfaces. *J. Micromech. Microeng.* **2005**, *15*, 691.

(188) Song, Z.; McElvany, C. L.; Phillips, A. B.; Celik, I.; Krantz, P. W.; Waththage, S. C.; Liyanage, G. K.; Apul, D.; Heben, M. J. A Technoeconomic Analysis of Perovskite Solar Module Manufacturing with Low-Cost Materials and Techniques. *Energy Environ. Sci.* **2017**, *10*, 1297–1305.

(189) Yang, Z.; Zhang, S.; Li, L.; Chen, W. Research Progress on Large-Area Perovskite Thin Films and Solar Modules. *J. Materiomics* **2017**, *3*, 231–244.

(190) Ono, L. K.; Park, N.-G.; Zhu, K.; Huang, W.; Qi, Y. Perovskite Solar Cells—Towards Commercialization. *ACS Energy Lett.* **2017**, *2*, 1749–1751.

(191) Berry, J. J.; van de Lagemaat, J.; Al-Jassim, M. M.; Kurtz, S.; Yan, Y.; Zhu, K. Perovskite Photovoltaics: The Path to a Printable Terawatt-Scale Technology. *ACS Energy Lett.* **2017**, *2*, 2540–2544.

(192) Lee, C.; Yan, H.; Brus, L. E.; Heinz, T. F.; Hone, J.; Ryu, S. Anomalous Lattice Vibrations of Single- and Few-Layer MoS<sub>2</sub>. *ACS Nano* **2010**, *4*, 2695–2700.

(193) Huang, Y.; Wu, J.; Hwang, K. C. Thickness of Graphene and Single-Wall Carbon Nanotubes. *Phys. Rev. B: Condens. Matter Mater. Phys.* **2006**, *74*, 245413.

(194) Novoselov, K. S.; Geim, A. K.; Morozov, S. V.; Jiang, D.; Zhang, Y.; Dubonos, S. V.; Grigorieva, I. V.; Firsov, A. A. Electric Field Effect in Atomically Thin Carbon Films. *Science* **2004**, *306*, 666–669.

(195) Baker, M. A.; Gilmore, R.; Lenardi, C.; Gissler, W. XPS Investigation of Preferential Sputtering of S from MoS<sub>2</sub> and Determination of MoS<sub>x</sub> Stoichiometry from Mo and S Peak Positions. *Appl. Surf. Sci.* **1999**, *150*, 255–262.

(196) Lee, Y. H.; Zhang, X. Q.; Zhang, W.; Chang, M. T.; Lin, C. T.; Chang, K. D.; Yu, Y. C.; Wang, J. T. W.; Chang, C. S.; Li, L. J.; Lin, T. W. Synthesis of Large-Area MoS<sub>2</sub> Atomic Layers with Chemical Vapor Deposition. *Adv. Mater.* **2012**, *24*, 2320–2325.

(197) Weber, T.; Muijsers, J. C.; van Wolput, J. H. M. C.; Verhagen, C. P. J.; Niemantsverdriet, J. W. Basic Reaction Steps in the Sulfidation of Crystalline MoO<sub>3</sub> to MoS<sub>2</sub>, As Studied by X-Ray Photoelectron and Infrared Emission Spectroscopy. *J. Phys. Chem.* **1996**, *100*, 14144–14150.

(198) Najafi, L.; Bellani, S.; Oropesa-Nuñez, R.; Ansaldo, A.; Prato, M.; Castillo, A. E. D. R.; Bonaccorso, F. Engineered MoSe<sub>2</sub>-Based Heterostructures for Efficient Electrochemical Hydrogen Evolution Reaction. *Adv. Energy Mater.* **2018**, *8*, 1703212.

(199) Bonaccorso, F.; Colombo, L.; Yu, G.; Stoller, M.; Tozzini, V.; Ferrari, A. C.; Ruoff, R. S.; Pellegrini, V. Graphene, Related Two-Dimensional Crystals, and Hybrid Systems for Energy Conversion and Storage. *Science* **2015**, *347*, 1246501.

(200) Yang, D.; Velamakanni, A.; Bozoklu, G.; Park, S.; Stoller, M.; Piner, R. D.; Stankovich, S.; Jung, I.; Field, D. A.; Ventrone, C. A.; Ruoff, R. S. Chemical Analysis of Graphene Oxide Films after Heat and Chemical Treatments by X-Ray Photoelectron and Micro-Raman Spectroscopy. *Carbon* **2009**, *47*, 145–152.

(201) Dong, X.; Su, C.-Y.; Zhang, W.; Zhao, J.; Ling, Q.; Huang, W.; Chen, P.; Li, L.-J. Ultra-Large Single-Layer Graphene Obtained from Solution Chemical Reduction and Its Electrical Properties. *Phys. Chem. Chem. Phys.* **2010**, *12*, 2164–2169.

(202) Becerril, H. A.; Stoltenberg, R. M.; Tang, M. L.; Roberts, M. E.; Liu, Z.; Chen, Y.; Kim, D. H.; Lee, B.-L.; Lee, S.; Bao, Z. Fabrication and Evaluation of Solution-Processed Reduced Graphene Oxide Electrodes for P- and N-Channel Bottom-Contact Organic Thin-Film Transistors. *ACS Nano* **2010**, *4*, 6343–6352.

(203) Ganguly, A.; Sharma, S.; Papakonstantinou, P.; Hamilton, J. Probing the Thermal Deoxygenation of Graphene Oxide Using High-Resolution *In Situ* X-Ray-Based Spectroscopies. *J. Phys. Chem. C* **2011**, *115*, 17009–17019.

- (204) Gao, W.; Alemany, L. B.; Ci, L.; Ajayan, P. M. New Insights into the Structure and Reduction of Graphite Oxide. *Nat. Chem.* **2009**, *1*, 403.
- (205) Johnson, P. A.; Levicky, R. X-Ray Photoelectron Spectroscopy and Differential Capacitance Study of Thiol-Functional Polysiloxane Films on Gold Supports. *Langmuir* **2004**, *20*, 9621–9627.
- (206) Rodriguez, J. A.; Jirsak, T.; Freitag, A.; Hanson, J. C.; Larese, J. Z.; Chaturvedi, S. Interaction of SO<sub>2</sub> with CeO<sub>2</sub> and Cu/CeO<sub>2</sub> Catalysts: Photoemission, XANES and TPD Studies. *Catal. Lett.* **1999**, *62*, 113–119.
- (207) Lee, C. Y.; Le, Q. V.; Kim, C.; Kim, S. Y. Use of Silane-Functionalized Graphene Oxide in Organic Photovoltaic Cells and Organic Light-Emitting Diodes. *Phys. Chem. Chem. Phys.* **2015**, *17*, 9369–9374.
- (208) Konios, D.; Stylianakis, M. M.; Stratakis, E.; Kymakis, E. Dispersion Behaviour of Graphene Oxide and Reduced Graphene Oxide. *J. Colloid Interface Sci.* **2014**, *430*, 108–112.
- (209) Wang, S.; Zhang, Y.; Abidi, N.; Cabrales, L. Wettability and Surface Free Energy of Graphene Films. *Langmuir* **2009**, *25*, 11078–11081.
- (210) Jiménez Sandoval, S.; Yang, D.; Frindt, R. F.; Irwin, J. C. Raman Study and Lattice Dynamics of Single Molecular Layers of MoS<sub>2</sub>. *Phys. Rev. B: Condens. Matter Mater. Phys.* **1991**, *44*, 3955–3962.
- (211) Kopaczek, J.; Polak, M. P.; Scharoch, P.; Wu, K.; Chen, B.; Tongay, S.; Kudrawiec, R. Direct Optical Transitions at K- and H-Point of Brillouin Zone in Bulk MoS<sub>2</sub>, MoSe<sub>2</sub>, WS<sub>2</sub>, and WSe<sub>2</sub>. *J. Appl. Phys.* **2016**, *119*, 235705.
- (212) Cheiwchanchamnangij, T.; Lambrecht, W. R. L. Quasiparticle Band Structure Calculation of Monolayer, Bilayer, and Bulk MoS<sub>2</sub>. *Phys. Rev. B: Condens. Matter Mater. Phys.* **2012**, *85*, 205302.
- (213) Eda, G.; Yamaguchi, H.; Voiry, D.; Fujita, T.; Chen, M.; Chhowalla, M. Photoluminescence from Chemically Exfoliated MoS<sub>2</sub>. *Nano Lett.* **2011**, *11*, 5111–5116.
- (214) Zhang, H.; Lu, S. B.; Zheng, J.; Du, J.; Wen, S. C.; Tang, D. Y.; Loh, K. P. Molybdenum Disulfide (MoS<sub>2</sub>) as a Broadband Saturable Absorber for Ultra-Fast Photonics. *Opt. Express* **2014**, *22*, 7249–7260.
- (215) Gan, Z. X.; Liu, L. Z.; Wu, H. Y.; Hao, Y. L.; Shan, Y.; Wu, X. L.; Chu, P. K. Quantum Confinement Effects across Two-Dimensional Planes in MoS<sub>2</sub> Quantum Dots. *Appl. Phys. Lett.* **2015**, *106*, 233113.
- (216) Dong, H. H.; Ju, H. D.; Seob, C. J.; Minsu, P.; Seok, S. T. Dual Role of Blue Luminescent MoS<sub>2</sub> Quantum Dots in Fluorescence Resonance Energy Transfer Phenomenon. *Small* **2014**, *10*, 3858–3862.
- (217) Mukherjee, S.; Maiti, R.; Katiyar, A. K.; Das, S.; Ray, S. K. Novel Colloidal MoS<sub>2</sub> Quantum Dot Heterojunctions on Silicon Platforms for Multifunctional Optoelectronic Devices. *Sci. Rep.* **2016**, *6*, 29016.
- (218) Gan, Z.; Xu, H.; Hao, Y. Mechanism for Excitation-Dependent Photoluminescence from Graphene Quantum Dots and Other Graphene Oxide Derivates: Consensus, Debates and Challenges. *Nanoscale* **2016**, *8*, 7794–7807.
- (219) Gopalakrishnan, D.; Damien, D.; Li, B.; Gullappalli, H.; Pillai, V. K.; Ajayan, P. M.; Shaijumon, M. M. Electrochemical Synthesis of Luminescent MoS<sub>2</sub> Quantum Dots. *Chem. Commun.* **2015**, *51*, 6293–6296.
- (220) Tauc, J. Optical Properties and Electronic Structure of Amorphous Ge and Si. *Mater. Res. Bull.* **1968**, *3*, 37–46.
- (221) Pankove, J. I.; Kiewit, D. A. Optical Processes in Semiconductors. *J. Electrochem. Soc.* **1972**, *5*, 156C–156C.
- (222) Mague, J. T. *Gmelin Handbook of Inorganic Chemistry*, 8th ed.; Rh Organometallics, 1984.
- (223) Li, T.; Galli, G. Electronic Properties of MoS<sub>2</sub> Nanoparticles. *J. Phys. Chem. C* **2007**, *111*, 16192–16196.
- (224) Lebegue, S.; Eriksson, O. Electronic Structure of Two-Dimensional Crystals from *Ab Initio* Theory. *Phys. Rev. B: Condens. Matter Mater. Phys.* **2009**, *79*, 115409.
- (225) Splendiani, A.; Sun, L.; Zhang, Y.; Li, T.; Kim, J.; Chim, C.-Y.; Galli, G.; Wang, F. Emerging Photoluminescence in Monolayer MoS<sub>2</sub>. *Nano Lett.* **2010**, *10*, 1271–1275.
- (226) Feng, Y.; Lin, S.; Huang, S.; Shrestha, S.; Conibeer, G. Can Tauc Plot Extrapolation Be Used for Direct-Band-Gap Semiconductor Nanocrystals? *J. Appl. Phys.* **2015**, *117*, 125701.
- (227) Hao, H.; Cuicui, D.; Hongyan, S.; Xun, F.; Jin, L.; Yanlei, T.; Wenbo, S. Water-Soluble Monolayer Molybdenum Disulfide Quantum Dots with Upconversion Fluorescence. *Part. Part. Syst. Charact.* **2015**, *32*, 72–79.
- (228) Sun, Y.; Takacs, C. J.; Cowan, S. R.; Seo, J. H.; Gong, X.; Roy, A.; Heeger, A. J. Efficient, Air-Stable Bulk Heterojunction Polymer Solar Cells Using MoO<sub>x</sub> as the Anode Interfacial Layer. *Adv. Mater.* **2011**, *23*, 2226–2230.
- (229) Kröger, M.; Hamwi, S.; Meyer, J.; Riedl, T.; Kowalsky, W.; Kahn, A. Role of the Deep-Lying Electronic States of MoO<sub>3</sub> in the Enhancement of Hole-Injection in Organic Thin Films. *Appl. Phys. Lett.* **2009**, *95*, 123301.
- (230) Balis, N.; Stratakis, E.; Kymakis, E. Graphene and Transition Metal Dichalcogenide Nanosheets as Charge Transport Layers for Solution Processed Solar Cells. *Mater. Today* **2016**, *19*, S80–S94.
- (231) Agresti, A.; Pescetelli, S.; Najafi, L.; Del Rio Castillo, A. E.; Oropesa-Nuñez, R.; Busby, Y.; Bonaccorso, F.; Di Carlo, A. Graphene and Related 2D Materials for High Efficient and Stable Perovskite Solar Cells. In *2017 IEEE 17th International Conference on Nanotechnology (IEEE-NANO)*; 2017; pp 145–150.
- (232) Lin, Q.; Armin, A.; Nagiri, R. C. R.; Burn, P. L.; Meredith, P. Electro-Optics of Perovskite Solar Cells. *Nat. Photonics* **2015**, *9*, 106.
- (233) Greiner, M. T.; Lu, Z.-H. Thin-Film Metal Oxides in Organic Semiconductor Devices: Their Electronic Structures, Work Functions and Interfaces. *NPG Asia Mater.* **2013**, *5*, e55.
- (234) Tress, W.; Marinova, N.; Moehl, T.; Zakeeruddin, S. M.; Nazeeruddin, M. K.; Grätzel, M. Understanding the Rate-Dependent J-V Hysteresis, Slow Time Component, and Aging in CH<sub>3</sub>NH<sub>3</sub>PbI<sub>3</sub> Perovskite Solar Cells: The Role of a Compensated Electric Field. *Energy Environ. Sci.* **2015**, *8*, 995–1004.
- (235) Zhao, Y.; Liang, C.; Zhang, H.; Li, D.; Tian, D.; Li, G.; Jing, X.; Zhang, W.; Xiao, W.; Liu, Q.; Zhang, F. Anomalous Large Interface Charge in Polarity-Switchable Photovoltaic Devices: An Indication of Mobile Ions in Organic-Inorganic Halide Perovskites. *Energy Environ. Sci.* **2015**, *8*, 1256–1260.
- (236) Elumalai, N. K.; Uddin, A. Hysteresis in Organic-Inorganic Hybrid Perovskite Solar Cells. *Sol. Energy Mater. Sol. Cells* **2016**, *157*, 476–509.
- (237) Chen, B.; Yang, M.; Priya, S.; Zhu, K. Origin of J–V Hysteresis in Perovskite Solar Cells. *J. Phys. Chem. Lett.* **2016**, *7*, 905–917.
- (238) Jiménez-López, J.; Cambarau, W.; Cabau, L.; Palomares, E. Charge Injection, Carriers Recombination and HOMO Energy Level Relationship in Perovskite Solar Cells. *Sci. Rep.* **2017**, *7*, 6101.
- (239) Docampo, P.; Ball, J. M.; Darwich, M.; Eperon, G. E.; Snaith, H. J. Efficient Organometal Trihalide Perovskite Planar-Heterojunction Solar Cells on Flexible Polymer Substrates. *Nat. Commun.* **2013**, *4*, 2761.
- (240) Bhosale, J. S.; Moore, J. E.; Wang, X.; Bermel, P.; Lundstrom, M. S. Steady-State Photoluminescent Excitation Characterization of Semiconductor Carrier Recombination. *Rev. Sci. Instrum.* **2016**, *87*, 13104.
- (241) Chang, L.; Kai, W.; Pengcheng, D.; Chao, Y.; Tianyu, M.; Xiong, G. Efficient Solution-Processed Bulk Heterojunction Perovskite Hybrid Solar Cells. *Adv. Energy Mater.* **2015**, *5*, 1402024.
- (242) Wang, X.; Bhosale, J.; Moore, J.; Kapadia, R.; Bermel, P.; Javey, A.; Lundstrom, M. Photovoltaic Material Characterization With Steady State and Transient Photoluminescence. *IEEE J. Photovolt.* **2015**, *5*, 282–287.
- (243) Ginger, D. S.; Greenham, N. C. Photoinduced Electron Transfer from Conjugated Polymers to CdSe Nanocrystals. *Phys. Rev. B: Condens. Matter Mater. Phys.* **1999**, *59*, 10622–10629.

- (244) Domanski, K.; Correa-Baena, J.-P.; Mine, N.; Nazeeruddin, M. K.; Abate, A.; Saliba, M.; Tress, W.; Hagfeldt, A.; Grätzel, M. Not All That Glitters Is Gold: Metal-Migration-Induced Degradation in Perovskite Solar Cells. *ACS Nano* **2016**, *10*, 6306–6314.
- (245) Park, N.-G.; Grätzel, M.; Miyasaka, T.; Zhu, K.; Emery, K. Towards Stable and Commercially Available Perovskite Solar Cells. *Nat. Energy* **2016**, *1*, 16152.
- (246) Wang, D.; Wright, M.; Elumalai, N. K.; Uddin, A. Stability of Perovskite Solar Cells. *Sol. Energy Mater. Sol. Cells* **2016**, *147*, 255–275.
- (247) Qin, X.; Zhao, Z.; Wang, Y.; Wu, J.; Jiang, Q.; You, J. Recent Progress in Stability of Perovskite Solar Cells. *J. Semicond.* **2017**, *38*, 11002.
- (248) Berhe, T. A.; Su, W.-N.; Chen, C.-H.; Pan, C.-J.; Cheng, J.-H.; Chen, H.-M.; Tsai, M.-C.; Chen, L.-Y.; Dubale, A. A.; Hwang, B.-J. Organometal Halide Perovskite Solar Cells: Degradation and Stability. *Energy Environ. Sci.* **2016**, *9*, 323–356.
- (249) Wang, Q.; Chen, B.; Liu, Y.; Deng, Y.; Bai, Y.; Dong, Q.; Huang, J. Scaling Behavior of Moisture-Induced Grain Degradation in Polycrystalline Hybrid Perovskite Thin Films. *Energy Environ. Sci.* **2017**, *10*, 516–522.
- (250) Han, Y.; Meyer, S.; Dkhissi, Y.; Weber, K.; Pringle, J. M.; Bach, U.; Spiccia, L.; Cheng, Y.-B. Degradation Observations of Encapsulated Planar CH<sub>3</sub>NH<sub>3</sub>PbI<sub>3</sub> Perovskite Solar Cells at High Temperatures and Humidity. *J. Mater. Chem. A* **2015**, *3*, 8139–8147.
- (251) Bryant, D.; Aristidou, N.; Pont, S.; Sanchez-Molina, I.; Chotchunangatchaval, T.; Wheeler, S.; Durrant, J. R.; Haque, S. A. Light and Oxygen Induced Degradation Limits the Operational Stability of Methylammonium Lead Triiodide Perovskite Solar Cells. *Energy Environ. Sci.* **2016**, *9*, 1655–1660.
- (252) Aristidou, N.; Sanchez-Molina, I.; Chotchunangchuchaval, T.; Brown, M.; Martinez, L.; Rath, T.; Haque, S. A. The Role of Oxygen in the Degradation of Methylammonium Lead Trihalide Perovskite Photoactive Layers. *Angew. Chem.* **2015**, *127*, 8326–8330.
- (253) Pearson, A. J.; Eperon, G. E.; Hopkinson, P. E.; Habisreutinger, S. N.; Wang, J. T.-W.; Snaith, H. J.; Greenham, N. C. Oxygen Degradation in Mesoporous Al<sub>2</sub>O<sub>3</sub>/CH<sub>3</sub>NH<sub>3</sub>PbI<sub>3-x</sub>Cl<sub>x</sub> Perovskite Solar Cells: Kinetics and Mechanisms. *Adv. Energy Mater.* **2016**, *6*, 1600014.
- (254) Nie, W.; Blancon, J.-C.; Neukirch, A. J.; Appavoo, K.; Tsai, H.; Chhowalla, M.; Alam, M. A.; Sfeir, M. Y.; Katan, C.; Even, J.; Tretiak, S. Light-Activated Photocurrent Degradation and Self-Healing in Perovskite Solar Cells. *Nat. Commun.* **2016**, *7*, 11574.
- (255) Docampo, P.; Bein, T. A Long-Term View on Perovskite Optoelectronics. *Acc. Chem. Res.* **2016**, *49*, 339–346.
- (256) Conings, B.; Drijkoningen, J.; Gauquelin, N.; Babayigit, A.; D'Haen, J.; D'Olieslaeger, L.; Ethirajan, A.; Verbeeck, J.; Manca, J.; Mosconi, E.; De Angelis, F. Intrinsic Thermal Instability of Methylammonium Lead Trihalide Perovskite. *Adv. Energy Mater.* **2015**, *5*, 1500477.
- (257) Juarez-Perez, E. J.; Hawash, Z.; Raga, S. R.; Ono, L. K.; Qi, Y. Thermal Degradation of CH<sub>3</sub>NH<sub>3</sub>PbI<sub>3</sub> Perovskite into NH<sub>3</sub> and CH<sub>3</sub>I Gases Observed by Coupled Thermogravimetry-Mass Spectrometry Analysis. *Energy Environ. Sci.* **2016**, *9*, 3406–3410.
- (258) Qiu, L.; Ono, L. K.; Qi, Y. Advances and Challenges to the Commercialization of Organic–inorganic Halide Perovskite Solar Cell Technology. *Mater. Today Energy* **2018**, *7*, 169–189.
- (259) Slavney, A. H.; Smaha, R. W.; Smith, I. C.; Jaffe, A.; Umeyama, D.; Karunadasa, H. I. Chemical Approaches to Addressing the Instability and Toxicity of Lead–Halide Perovskite Absorbers. *Inorg. Chem.* **2017**, *56*, 46–55.
- (260) McMeekin, D. P.; Sadoughi, G.; Rehman, W.; Eperon, G. E.; Saliba, M.; Hörantner, M. T.; Haghighirad, A.; Sakai, N.; Korte, L.; Rech, B.; Johnston, M. B. A Mixed-Cation Lead Mixed-Halide Perovskite Absorber for Tandem Solar Cells. *Science* **2016**, *351*, 151–155.
- (261) Saliba, M.; Matsui, T.; Seo, J.-Y.; Domanski, K.; Correa-Baena, J.-P.; Nazeeruddin, M. K.; Zakeeruddin, S. M.; Tress, W.; Abate, A.; Hagfeldt, A.; Grätzel, M. Cesium-Containing Triple Cation Perovskite Solar Cells: Improved Stability, Reproducibility and High Efficiency. *Energy Environ. Sci.* **2016**, *9*, 1989–1997.
- (262) Saliba, M.; Matsui, T.; Domanski, K.; Seo, J.-Y.; Ummadisingu, A.; Zakeeruddin, S. M.; Correa-Baena, J.-P.; Tress, W. R.; Abate, A.; Hagfeldt, A.; Grätzel, M. Incorporation of Rubidium Cations into Perovskite Solar Cells Improves Photovoltaic Performance. *Science* **2016**, *354*, 206–209.
- (263) Busby, Y.; Agresti, A.; Pescetelli, S.; Di Carlo, A.; Noel, C.; Pireaux, J.-J.; Houssiau, L. Aging Effects in Interface-Engineered Perovskite Solar Cells with 2D Nanomaterials: A Depth Profile Analysis. *Mater. Today Energy* **2018**, *9*, 1–10.
- (264) Jiangwei, L.; Qingshun, D.; Nan, L.; Liduo, W. Direct Evidence of Ion Diffusion for the Silver-Electrode-Induced Thermal Degradation of Inverted Perovskite Solar Cells. *Adv. Energy Mater.* **2017**, *7*, 1602922.
- (265) Cacovich, S.; Cina, L.; Matteocci, F.; Divitini, G.; Midgley, P. A.; Di Carlo, A.; Ducati, C. Gold and Iodine Diffusion in Large Area Perovskite Solar Cells under Illumination. *Nanoscale* **2017**, *9*, 4700–4706.
- (266) Capasso, A.; Matteocci, F.; Najafi, L.; Prato, M.; Buha, J.; Cina, L.; Pellegrini, V.; Di Carlo, A.; Bonaccorso, F. Few-Layer MoS<sub>2</sub> Flakes as Active Buffer Layer for Stable Perovskite Solar Cells. *Adv. Energy Mater.* **2016**, *6*, 1600920.
- (267) Taheri, B.; Nia, N. Y.; Agresti, A.; Pescetelli, S.; Ciceroni, C.; Castillo, A. E. D. R.; Cina, L.; Bellani, S.; Bonaccorso, F.; Di Carlo, A. Graphene-Engineered Automated Sprayed Mesoscopic Structure for Perovskite Device Scaling-Up. *2D Mater.* **2018**, DOI: 10.1088/2053-1583/aad983.
- (268) Reese, M. O.; Gevorgyan, S. A.; Jørgensen, M.; Bundgaard, E.; Kurtz, S. R.; Ginley, D. S.; Olson, D. C.; Lloyd, M. T.; Morvillo, P.; Katz, E. A.; Elschner, A. Consensus Stability Testing Protocols for Organic Photovoltaic Materials and Devices. *Sol. Energy Mater. Sol. Cells* **2011**, *95*, 1253–1267.
- (269) Matteocci, F.; Cina, L.; Lamanna, E.; Cacovich, S.; Divitini, G.; Midgley, P. A.; Ducati, C.; Di Carlo, A. Encapsulation for Long-Term Stability Enhancement of Perovskite Solar Cells. *Nano Energy* **2016**, *30*, 162–172.
- (270) Matteocci, F.; Busby, Y.; Pireaux, J.-J.; Divitini, G.; Cacovich, S.; Ducati, C.; Di Carlo, A. Interface and Composition Analysis on Perovskite Solar Cells. *ACS Appl. Mater. Interfaces* **2015**, *7*, 26176–26183.
- (271) Petridis, C.; Kakavelakis, G.; Kymakis, E. Renaissance of Graphene-Related Materials in Photovoltaics due to the Emergence of Metal Halide Perovskite Solar Cells. *Energy Environ. Sci.* **2018**, *11*, 1030–1061.
- (272) Reese, M. O.; Dameron, A. A.; Kempe, M. D. Quantitative Calcium Resistivity Based Method for Accurate and Scalable Water Vapor Transmission Rate Measurement. *Rev. Sci. Instrum.* **2011**, *82*, 85101.